Building and Environment 266 (2024) 112071

Contents lists available at ScienceDirect

Building and Environment

journal homepage: www.elsevier.com/locate/buildenv

A panorama-based technique to estimate sky view factor and solar irradiance considering transmittance of tree canopies

Kunihiko Fujiwara [a,b], Koichi Ito [a], Marcel Ignatius [a,c], Filip Biljecki [a,d,*]

[a] Department of Architecture, National University of Singapore, 4 Architecture Drive, Singapore, 117566, Singapore
[b] Research & Development Institute, Takenaka Corporation, 1-5-1 Otsuka, Inzai, Chiba, 270-1352, Japan
[c] Department of the Built Environment, National University of Singapore, 4 Architecture Drive, Singapore, 117566, Singapore
[d] Department of Real Estate, National University of Singapore, 15 Kent Ridge Drive, Singapore, 119245, Singapore

ARTICLE INFO

Dataset link: https://github.com/kunifujiwara/TreeShadeMapper, https://pypi.org/project/tree-shade-mapper/

Keywords:
Shading effect
Sky visibility
Tree crown
Sunlight penetration
Street view imagery
Computer vision
Solar radiation

ABSTRACT

Street-view-based techniques for assessing the sky view factor (SVF) and solar irradiance under trees are gaining attention as tools for evaluating trees as nature-based solutions to mitigate urban heat risks. Although these metrics significantly depend on the morphology of trees and resulting canopy transmittance, an existing approach, termed the Solid Canopy Method (SCM), assumes zero transmission and has not accounted for these variations. This paper advances the computation of both metrics, improving their accuracy and application — we developed the Transmissive Canopy Method (TCM), a panorama-based approach that integrates semantic segmentation and binarization to evaluate SVF and solar irradiance while accounting for transmittance of tree canopies. Using a study area on a university campus in Singapore, we collected data on solar irradiance and 360° imagery to validate our method. The results indicated improved accuracy with MAE, RMSE, and R^2 values of 77.8 Wm^{-2}, 105.0 Wm^{-2} and 0.90, respectively — significantly outperforming the SCM. We showcased two use cases of our method: (1) high-resolution mapping of SVF and solar irradiance in a field with trees, and (2) walking route optimization considering sunlight exposure. Our findings highlight the strong capability of our TCM to evaluate the effects of trees in mitigating urban heat more accurately than the existing method. Additionally, the TCM has potential applications in urban planning and management, enabling strategic tree planting prioritizing areas lacking sufficient shading and developing tools for optimizing walking routes to minimize sunlight exposure.

1. Introduction

The heat mitigation effects of trees have gained increasing attention due to concerns about urban heat caused by heat waves [1–4], climate change [5–7], and the urban heat island effect [8–11]. Trees offer various positive effects, including not only mitigating heat but also enhancing scenery, improving mental health and well-being [12,13], and promoting biodiversity [14–17]. These benefits underscore the significance of trees as a nature-based solution for developing sustainable cities [18,19]. The heat mitigation effects of trees include shading through their canopies [20–22] and cooling through transpiration [23–25], with shading being particularly critical to people's heat risk because of its significant influence on energy flux into human bodies [26–29]. High-resolution spatio-temporal data on the shading effects of trees are important for urban planners and policymakers to make informed decisions in planning urban greening initiatives. For example, such data can help identify parts of a region where tree shading is lacking and pedestrians are likely to be exposed to severe heat stress, and can assist in prioritizing such locations for tree planting [30,31].

The shading effect of trees primarily depends on morphological parameters of their canopies, such as the shapes of canopies and density, inclination, and shape of leaves, all of which affect the transmittance for solar radiation [32–34]. Previous studies have investigated the shading effect of trees using measurements of solar irradiance with pyranometers or through physical simulations with ray-tracing [35–38]. These methods enable us to obtain accurate solar irradiance data corresponding to the morphological parameters of trees. However, it is not feasible to install a large number of pyranometers to obtain high-resolution and extensive data on solar irradiance under tree canopies due to the high costs involved. Additionally, conducting accurate physical simulations of shading effects requires a detailed 3D model of tree canopies [39,40]. To acquire such detailed information, LiDAR measurements are necessary [41,42]; however, these are costly, thus limiting application and scalability.

* Corresponding author at: Department of Architecture, National University of Singapore, 4 Architecture Drive, Singapore, 117566, Singapore.
E-mail addresses: kunihiko@nus.edu.sg (K. Fujiwara), koichi.ito@u.nus.edu (K. Ito), m.ignatius@nus.edu.sg (M. Ignatius), filip@nus.edu.sg (F. Biljecki).

https://doi.org/10.1016/j.buildenv.2024.112071
Received 2 July 2024; Received in revised form 6 September 2024; Accepted 8 September 2024
Available online 13 September 2024

List of Abbreviations

GHI_{utc}	Global horizontal irradiance under tree canopies (Wm^{-2})
GHI_{rt}	Global horizontal irradiance on rooftops (Wm^{-2})
I_{dif}	Sky diffuse irradiance above tree canopies (Wm^{-2})
I_{dir}	Normal direct solar irradiance above tree canopies (Wm^{-2})
MAE	Mean Absolute Error
R^2	Coefficient of determination
RMSE	Root Mean Square Error
RT	Rooftop
SCM	Solid Canopy Method (previous method)
SVF	Sky View Factor
TCM	Transmissive Canopy Method (our proposed method)
UTC	Under Tree Canopy

Meanwhile, the sky view factor (SVF), defined as the ratio of visible sky within the upper hemispherical view of a certain location, is a significant factor for the solar irradiance [43,44]. The SVF of a location is directly proportional to diffuse solar irradiance absorbed on a horizontal surface at the location [45]. Additionally, the SVF is directly correlated with atmospheric radiation highlighting its importance in evaluating the thermal environment and associated heat risks [46,47]. The SVF also plays a crucial role in the perception of urban visual environments. Many studies have reported an association between the sky visibility and urban visual perceptions such as feelings of openness and oppressiveness [48–53].

To evaluate SVF under tree canopies, previous research has primarily used a binarization-based method with hemispherical fisheye photos [54–56] or physical simulations equipped with ray-tracing techniques [57–59]. In the binarization-based method, image binarization techniques are employed to separate 'sky' pixels from 'object' pixels that obstruct the view towards the sky [60,61]. This method is implemented by applying thresholds to certain parameters calculated from the pixel's RGB values. However, the variability of optimal thresholds, depending on tree species, materials of surrounding buildings, weather conditions, and the resulting light environment, poses challenges in scalability and limits broader practical applications. Additionally, physical simulations of the SVF require detailed 3D models of tree canopies, which similarly hinders scaled practical usages, as is the case with solar irradiance studies.

Meanwhile, an approach using street-level panoramas is gaining attention as a potential alternative to existing methods for evaluating SVF and solar irradiance under tree canopies [62–66]. In this approach, semantic segmentation – a computer vision technique used to classify each pixel in an image and assign it to a specific object class (Figs. 1 and 2) – of a street-level panorama is conducted to calculate the SVF and solar irradiance. The sun position is localized on the segmented panorama to determine the presence of shading objects that block direct solar radiation. If no shading objects are present, the global irradiance is calculated as the sum of direct and diffuse irradiance, the latter being determined by the SVF. If shading objects exist, the global irradiance is calculated as equivalent to diffuse irradiance alone. However, this approach has room for improving accuracy, as it currently treats the tree canopy, which actually includes sky visible between leaves, merely as an 'object' area with zero transmittance, not considering any potential solar radiation passage through the canopies.

Therefore, this research proposes a novel method that estimates the SVF and solar irradiance considering the transmittance of tree canopies, advancing the current approaches that use street-level panoramas. More specifically, we develop a method that calculates transmittance by combining semantic segmentation and binarization of panoramic imagery and uses this calculated transmittance to estimate SVF and solar irradiance (Fig. 1). The accuracy of our proposed method is validated through the collection of solar irradiance data and panoramic imagery. Additionally, we demonstrate two use cases that rely on our proposed method: (1) creating two-dimensional high-resolution maps for SVF and solar irradiance; and (2) optimizing walking routes based on cumulative solar irradiance.

As a result, our research addresses the following research questions that advance the quantification of the contribution of trees in the built environment and visual landscape: 'How can we use panoramas to accurately estimate transmittance?'; 'How does the consideration of transmittance impact on the SVF under tree canopies?'; 'Can the consideration of transmittance contribute to improving accuracy for estimating solar irradiance under tree canopies?'; 'How does the consideration of transmittance improve the accuracy compared to previous methods?'; 'How can high-resolution maps of SVF and solar irradiance under trees be utilized for practical applications?'

2. Background and related work

2.1. Evaluation of solar irradiance

Solar irradiance is a significant factor in heat stress, influencing comfort and heat risks associated with outdoor activities [67,68]. Consequently, it has been evaluated for various purposes, including assessing heat risks at construction sites [69], enhancing area walkability [70,71], improving thermal comfort in urban open spaces [72,73], and reducing the risk of skin cancer [74]. Additionally, solar irradiance is critical for estimating power generation through photovoltaic panels [75,76]. To assess solar irradiance under tree canopies, there are mainly two methods: measurement and physical simulation.

For measuring solar irradiance under trees, many studies have utilized pyranometers [77–83]. By comparing solar irradiance in shaded areas with that at reference locations in sunlit areas, the shading effect of tree canopies can be evaluated. Takács et al. [81] and Yoshida et al. [82] have reported on the impact of differences in tree species and resulting leaf density on shading effects. Additionally, Nishikawa and Shukuya [83] has noted the impact of tree health and resulting leaf density on shading. Such measurements, considering the diverse conditions of tree canopies, provide an accurate evaluation of solar irradiance. However, obtaining spatio-temporally high-resolution data requires dense measurement points and significant equipment costs. Some studies have employed traverse measurements using mobile weather stations to increase spatial coverage [84,8]; however, increasing temporal coverage remains challenging.

Meanwhile, many studies have utilized physical simulations with ray-tracing to calculate the shading effects of tree canopies and resulting solar irradiance beneath them [85–87]. For example, Kumakura et al. [88] simulated the process of solar radiation transfer within tree canopies using a ray-tracing method and 3D models of trees that reproduced all individual leaves and branches. In parallel, many studies have calculated radiation transfer within tree canopies by computing transmittance using functions that consider leaf density and the penetration distance of solar radiation [89–91]. Physical simulation can provide solar irradiance data at a high spatio-temporal resolution if it employs an adequate mesh size and time step. However, this method requires 3D models of tree canopies with detailed morphological parameters, including the shape of the canopies, the density, orientation, inclination, and shape of leaves, which are not readily available in many cases.

In summary, both primary methods – measurement and simulation – face scalability challenges due to the high cost of equipment and the lack of available input data.

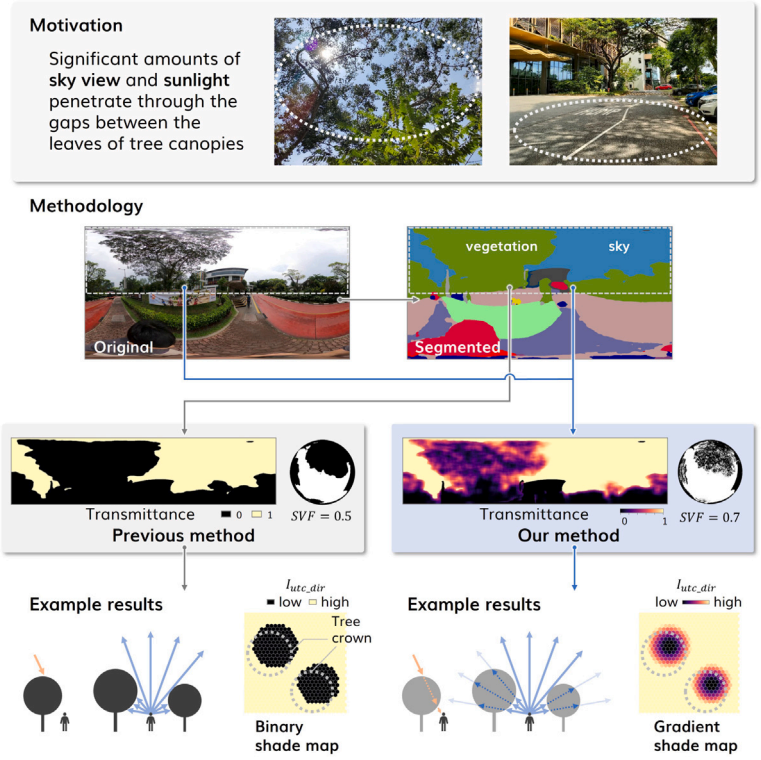

Fig. 1. Conceptual diagram illustrating the differences between the previous method and our proposed method, including the benefit for use cases. In the shade maps, I_{utc_dir} represents the direct horizontal irradiance under tree canopies (Wm^{-2}). These maps display the horizontal and two-dimensional distribution of I_{utc_dir} with the assumption that I_{utc_dir} is calculated at multiple locations by the previous method (left) and by our method (right).

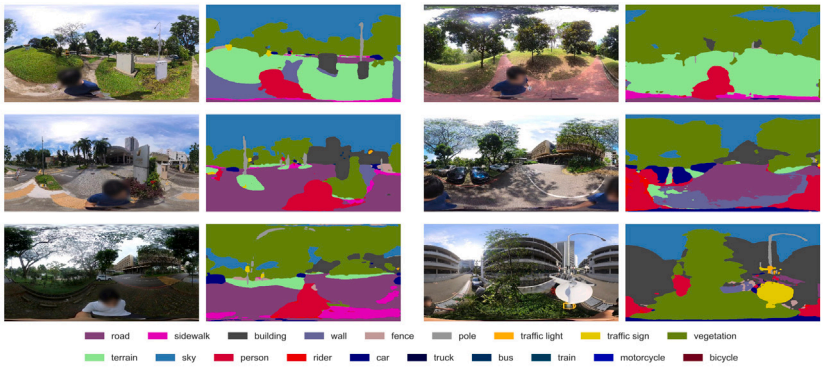

Fig. 2. Examples of segmentation results.

2.2. Evaluation of sky view factor

The SVF is defined as the ratio of the sky that is unobstructed by objects when viewed from a specific point. More specifically, it refers to the ratio of sky visible in an orthographic projection of the upper hemisphere. The SVF is a crucial parameter for urban microclimate and is directly used to calculate diffuse solar irradiance [43–45]. Additionally, the SVF has been used to assess pedestrians' visual perceptions of streetscapes [92]. To evaluate the SVF, methods typically involve using binarization of photography or physical simulation with ray-tracing [43,93,60].

The binarization-based method requires the binarization of upper hemispherical photos in orthographic projection [93,60,94]. It binarizes the photos based on the brightness values, which are determined from the RGB values, of each pixel to distinguish between 'sky' and 'object' pixels. The SVF is then evaluated based on the ratio of sky pixels. However, if the photo captures objects that are brighter than the sky, the binarization process may mistakenly recognize object pixels as sky [94]. To prevent this from resulting in lower accuracy, manual labeling of such objects is required, which can be labor-intensive in large-scale measurements.

The physical simulation uses ray-tracing and 3D models of urban geometry, including buildings and trees [95,57,58,96]. In this approach, a specific number of virtual rays are emitted in upper hemispherical directions from a target point, and the ratio of rays that are unobstructed by objects and reach the upper or side boundary of the calculation area is calculated as SVF. Similar to physical simulations for solar irradiance, this method requires 3D models of tree canopies with detailed morphological information, which necessitates expensive LiDAR measurements.

Similar to the evaluation of solar irradiance, the two primary methods for assessing SVF encounter scalability challenges due to the manual efforts required and the high costs associated with data acquisition.

2.3. Transmittance and morphological features of tree canopies

Transmittance for solar radiation through tree canopies is primarily determined by leaf density, which can be quantified by point cloud data of leaves from Light Detection and Ranging (LiDAR) surveys [97–105]. Some studies have leveraged LiDAR not only to obtain information about leaf density but also about the orientation and inclination of leaves, which influence transmittance [106–109]. While LiDAR provides detailed and comprehensive information on the structures of tree canopies, it faces scalability challenges due to high equipment costs and the limited availability of open and crowdsourced data providers.

Another method for calculating leaf density involves the binarization of upward hemispherical photography captured under tree canopies [110–112]. This method estimates leaf density based on the ratio of black pixels, which represent the leaves and branches of tree canopies.

Meanwhile, in addition to tree canopies, various types of shades feature perforated or porous structures, including pergolas [113,114] and louvers [115,116]. The presence of these diverse shading objects with transmissive properties in built environments underscores the importance of developing scalable and accurate methods to estimate transmittance.

2.4. Related work

Many previous studies have utilized geo-tagged street-level panoramas to estimate solar irradiance [62–65]. Their methods usually start with conducting semantic segmentation to detect shading objects, such as trees and buildings. They then calculate the SVF and diffuse solar irradiance, localize the temporal sun position for each time of day on segmented panoramic imagery, assess whether direct solar radiation was shaded, and calculate direct solar irradiance. The global solar irradiance is obtained as the sum of the diffuse and direct solar irradiance. Similarly, Li and Ratti [117] employed street-view panoramas to calculate sunlight hours, indicating the total duration each day that a particular location is exposed to direct solar irradiance.

These segmentation-based methods offer scalability advantages due to the availability of various data sources. Several commercial and crowdsourced providers offer panoramic imagery, including Google Street View, Baidu Map, Mapillary, and KartaView [66,118]. Moreover, collecting one's own dataset using a panoramic camera has become increasingly feasible and cost-effective. In fact, many studies have utilized panoramic imagery that they have collected themselves [119–122].

To date, no semantic segmentation models have been detailed enough to identify the small sky-visible areas between leaves within tree canopies as 'sky' areas. Consequently, these segmentation-based methods have classified pixels in broad strokes, recognizing tree canopies – which actually contain a mix of sky, leaves, and branches – merely as 'object' areas. Additionally, these methods have not accounted for the transmittance of tree canopies, thus assuming a transmittance value of zero. However, as previously mentioned, the transmittance of tree canopies can vary significantly depending on morphological factors such as canopy shapes and leaf density. Therefore, incorporating transmittance considerations is expected to substantially improve the accuracy of estimations for SVF and solar irradiance.

Meanwhile, several studies employed the binarization of hemispherical photography to estimate SVF and solar irradiance [94,123,124]. Kou et al. [125] used binarization of street view panoramas to evaluate the visibility of global navigation satellites, a concept similar to the visibility of the sun or the presence of direct solar radiation. Additionally, Jonas et al. [126] applied binarization on a hemispherical photograph to assess the transmittance of solar radiation through tree canopies.

One of the primary challenges in using binarization to calculate SVF and solar irradiance involves setting optimal thresholds to distinguish sky pixels. This task is complicated due to the variability of RGB values of sky pixels and those of object pixels – including tree canopies and buildings – which can change depending on weather conditions, light environments, tree species, and building materials. Zeng et al. [94] and Kou et al. [125] attempted to automate thresholding to account for such variability in urban environments, employing Otsu's method [127]. This method automatically determines a threshold that maximizes the variance of pixel values between two classes and is particularly effective when the image consists of two dominant elements with two distinct colors. However, its accuracy in extracting sky in complex urban environments, which consist of diverse elements, is limited. For instance, Liu et al. [123] observed the misrecognition of brighter building surfaces as sky pixels. To address this issue, they implemented post-processing corrections, where misidentified sky pixels surrounded by object pixels were reassigned to object pixels. However, this approach inadvertently led to the misidentification of sky pixels between leaves within tree canopies as object pixels. Zeng et al. [94] and Kou et al. [125] provided examples showing that the visible sky between leaves was labeled as object pixels. Liu et al. [123] employed a clustering-based binarization method, while Middel et al. [124] used an edge-detection-based approach. Both studies yielded similar results where sky pixels between tree canopies were labeled as object pixels. It is important to note that their research did not focus on the transmittance of tree canopies and would have considered such an underestimation of transmittance as a minor error.

As mentioned above, Jonas et al. [126] used binarization while considering transmission through tree canopies. However, their study area was situated in a forest, and they did not address the complexities of urban environments. Furthermore, their analysis was based on a single hemispherical photo captured from one location, and they did not employ any automated method for thresholding.

To address these challenges in both segmentation-based and binarization-based methods, we find potential solutions in the combination of segmentation and binarization. Semantic segmentation, which can extract object pixels independently of the brightness of the pixels, and binarization, which enables detailed pixel-scale classification of sky and object pixels within tree canopies, should be able to complement each other. Furthermore, for a robust and automated method to binarize pixels, extracting pixels of sky and tree canopies by using semantic segmentation results and analyzing the pixel values would help determine proper thresholds.

Therefore, we present a method featuring two primary contributions to the literature. First, we propose a novel approach that combines semantic segmentation and binarization to calculate the SVF and solar irradiance, considering the transmittance of tree canopies. Second, we develop a new method to automatically determine the optimal thresholds for binarizing sky and object pixels within tree canopies, using results of semantic segmentation and considering diverse environmental conditions.

3. Methodology

In this study, we propose a panorama-based method to evaluate SVF and solar irradiance while accounting for the transmittance of tree canopies, which varies depending on tree species and health conditions. Hereafter, this approach is referred to as "Transmissive Canopy Method (TCM)". In this section, we elaborate on the individual calculation subprocesses involved in the TCM.

3.1. Transmittance and sky view factor

We estimate transmittance by combining semantic segmentation and binarization of panoramic imagery. As shown in Fig. 3, the workflow consists of three main steps: (1) semantic segmentation, (2) binarization, and (3) post-processing of the binarized imagery, which includes kernel averaging, orthographic projection, and pixel ratio calculation. The following subsections elaborate on these steps.

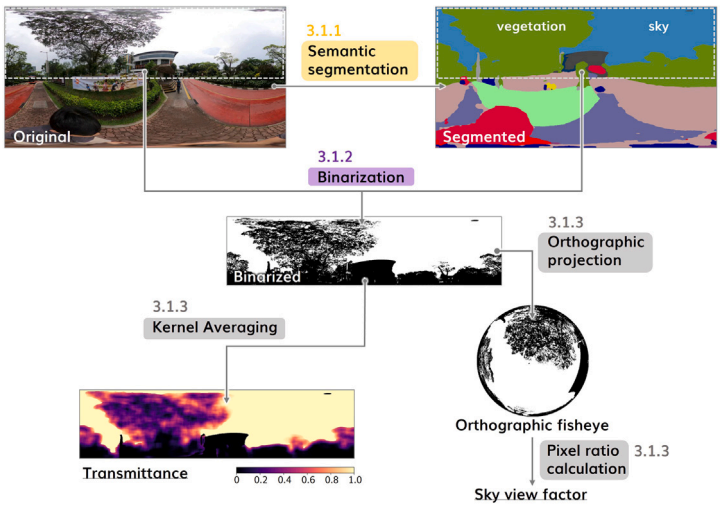

Fig. 3. Workflow diagram for calculating transmittance. Black pixels in binarized images represent 'object', while white pixels represent 'sky'.

3.1.1. Semantic segmentation

Semantic segmentation is a technique of computer vision that classifies each pixel of an image into a specific semantic class, such as 'sky', 'vegetation', or 'building'. This enables the estimation of the proportion of each semantic class within the image. The technique has been widely adopted in urban studies due to its flexibility in quantifying streetscape features and its reliability and accuracy, which have significantly improved in recent years thanks to rapid advancements in deep learning models [62–65]. For our study, we utilize the Mask2Former model pretrained on the CityScapes dataset to conduct semantic segmentation of panoramic imagery. This transformer-based model achieves a mIoU of 84.5% across 19 categories [128,129] . The categories are (1) road, (2) sidewalk, (3) building, (4) wall, (5) fence, (6) pole, (7) traffic light, (8) traffic sign, (9) vegetation, (10) terrain, (11) sky, (12) person, (13) rider, (14) car, (15) truck, (16) bus, (17) train, (18) motorcycle, (19) bicycle. Fig. 2 illustrates examples of the results. For our TCM, we specifically extract (9) vegetation and (11) sky. We use panoramic images of size 2048 × 1024 pixels for semantic segmentation. While we use the entire panorama in the segmentation process, we only use the upper half, which can influence the SVF and solar irradiance, in all subsequent processes.

3.1.2. Binarization

In our TCM, we conduct binarization to classify each pixel into 'sky' and 'object' using both an original and segmented panorama. The binarization process is carried out in accordance with Eqs. (1) and (2).

$$pb = \begin{cases} 0 & \text{if } ps \neq 9 \text{ (vegetation) and if } ps \neq 11 \text{ (sky)} \\ 1 & \text{if } ps = 11 \text{ (sky)} \\ 0 & \text{if } ps = 9 \text{ (vegetation) and if } pbr \leq X \\ 1 & \text{if } ps = 9 \text{ (vegetation) and if } pbr > X \end{cases} \quad (1)$$

$$pbr = \frac{0.5 \times R + G + 1.5 \times B}{3} \quad \text{(Kou et al. [125])} \quad (2)$$

Where: pb represents the binarization value for each pixel, with 1 representing 'sky' and 0 representing 'object'. ps represents the semantic segmentation category for each pixel, with 9 corresponding to 'vegetation' and 11 corresponding to 'sky'. pbr represents the brightness value for each pixel, serving as an indicator to determine whether a pixel represents 'object' or 'sky'. R, G, and B indicate the pixel values in the red, green, and blue channels, respectively. X is the threshold used to determine pb based on the value of pbr.

Based on Eq. (1), we initially assign a pb value of 0 (object) to pixels whose ps values are neither 9 (vegetation) nor 11 (sky). Pixels with a ps value of 11 (sky) are assigned a pb value of 1 (sky). Subsequently, we binarize the remaining pixels with a ps value of 9 (vegetation) using the brightness value of each pixel (pbr) and a binarization threshold X. The pbr is calculated using Eq. (2).

We determine X considering a mix of sky and leaves in pixels, termed 'mixels', which simultaneously capture both elements. As illustrated in Fig. 4, within a small patch of a tree canopy in a panoramic image, some pixels capture exclusively sky or leaves, while others capture a combination of both. To accurately evaluate transmittance, which varies depending on the type of trees, it is crucial to precisely calculate the percentage of gaps between leaves in panoramic imagery. Therefore, mixels predominantly featuring sky (more than 50%) should be classified as 'sky', and conversely, those predominantly featuring leaves (more than 50%) as 'object'. To identify the optimal X for this binarization, we analyze histogram peaks for the pbr values of pixels whose ps values are 9 (vegetation) or 11 (sky). This filtering of pixels using segmentation results helps reduce undesirable noise in the histogram analysis by focusing on sky and vegetation pixels. Fig. 5 illustrates histograms for pbr values created using example panoramas. As shown in Fig. 5, the pbr values for sky and vegetation pixels typically exhibit distinct ranges and peak values. The interval between these two peak values represents mixels of sky and leaves. Consequently, we use the midpoint of this interval as the X value for binarization. Different X values are determined for each panorama to accommodate variations in the surrounding environments, including weather, light conditions, tree species, and building materials.

3.1.3. Postprocessing of binarized imagery

We calculate the transmittance of each pixel by averaging pixel values within a 40 × 40 kernel. This averaging is intended to enhance the robustness of solar irradiance estimation against errors in the sun position. Without this averaging, the estimated values for solar irradiance under tree canopies would be significantly affected by small changes in sun position. Additionally, we calculate the SVF by transforming the upper half of the binarized panorama into an orthographic fisheye and then calculating the ratio of sky pixels within this transformed image.

3.2. Solar irradiance

To calculate solar irradiance under tree canopies, the TCM localizes sun positions and calculates solar radiation transfer, accounting for the transmittance and sky view factor obtained through the preprocessings steps described in Section 3.1. The following subsections provide details for each step in the solar irradiance calculation.

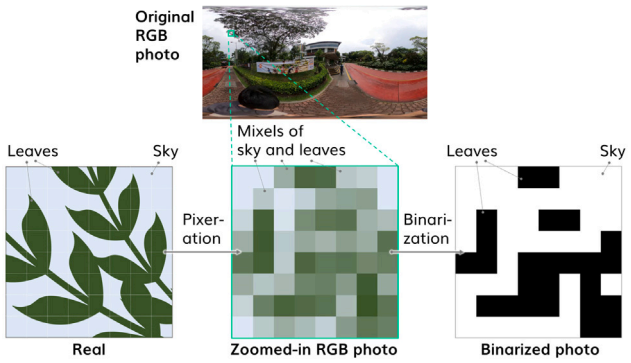

Fig. 4. Conceptual diagram illustrating the binarization of mixels into sky and object pixels.

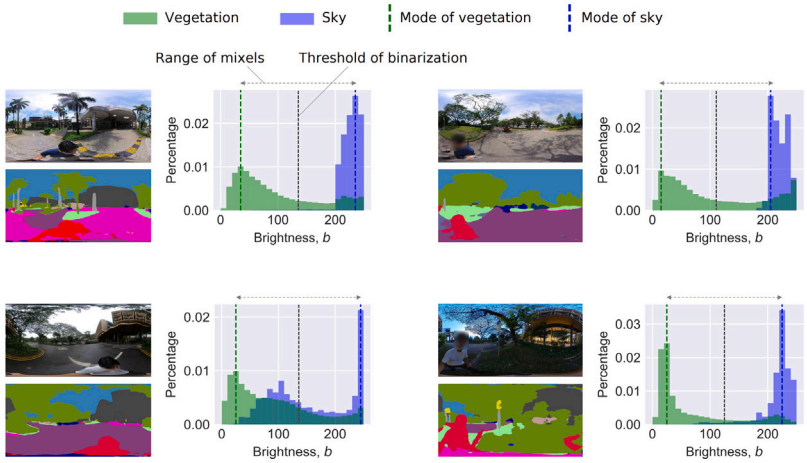

Fig. 5. Examples of histograms depicting brightness values for sky and vegetation pixels, accompanied by segmentation results. The legends in the segmentation results are the same as in Fig. 2.

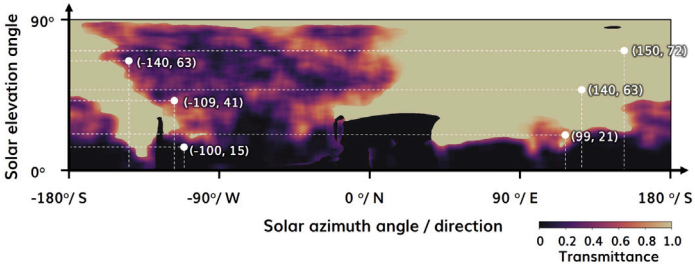

Fig. 6. Localization of sun positions in a panoramic image with calculated transmittance values.

3.2.1. Localization of sun position

Sun position is defined by two parameters: solar elevation and solar azimuth angle. These calculations are performed using 'pvlib' [130], a Python module primarily designed for estimating solar radiation gain on photovoltaic (PV) panels. In 'pvlib', the sun position is determined using geographical coordinates (latitude and longitude), date, and time as input parameters [131].

The sun position is then localized in a panoramic image of calculated transmittance values, as shown in Fig. 6. The localization is feasible because the x and y coordinates in a panoramic image with equirectangular projection correspond to the azimuth angle and the elevation angle, respectively. The transmittance value of the localized sun position is used in calculating solar irradiance, as detailed in Section 3.2.2.

3.2.2. Calculation of radiation transfer

The global horizontal irradiance under tree canopies (I_{utc} (Wm^{-2})) can be divided into three composing elements; direct solar irradiance (I_{utc_dir} (Wm^{-2})), sky diffuse solar irradiance (I_{utc_dif} (Wm^{-2})), and irradiance reflected from surrounding objects ($I_{utc\_obj\_ref}$ (Wm^{-2})). Fig. 7 illustrates the concept of these types of irradiance. Eqs. (3), (4), and (5), detail the calculation for each.

$$GHI_{utc} = I_{utc\_dir} + I_{utc\_dif} + I_{utc\_obj\_ref} \quad \text{(Heim and Knera [132])} \tag{3}$$

$$I_{utc\_dir} = \tau \cdot I_{dir} \cdot \sin e \quad \text{(Heim and Knera [132])} \tag{4}$$

$$I_{utc\_dif} = SVF \cdot I_{dif} \quad \text{(Heim and Knera [132])} \tag{5}$$

Where: GHI_{utc} is the global horizontal irradiance under tree canopies (Wm^{-2}). I_{utc_dir} is the direct horizontal irradiance under

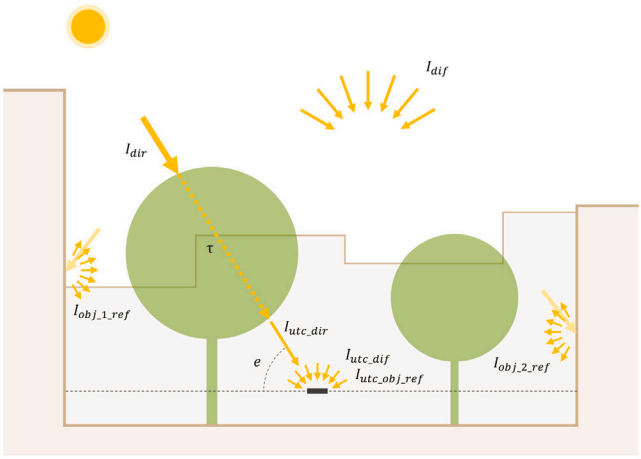

Fig. 7. Conceptual diagram illustrating the principal elements of solar irradiance in urban settings.

tree canopies (Wm^{-2}). I_{utc_dif} is the sky diffuse horizontal irradiance under tree canopies (Wm^{-2}). $I_{utc\_obj\_ref}$ is the horizontal irradiance reflected from surrounding objects (Wm^{-2}). τ is the transmittance of tree canopies for solar radiation. I_{dir} is the normal direct solar irradiance above tree canopies (Wm^{-2}). e is the solar elevation angle. SVF is the sky view factor. I_{dif} is the sky diffuse irradiance above tree canopies.

Several previous studies have reported that the magnitude of $I_{utc\_obj\_ref}$ is insignificant due to the low reflectance of basic materials of urban surfaces such as asphalt, concrete, soil, and vegetation, etc [132–135]. Consequently, many studies have omitted this value in the calculation of solar irradiance [117,63,64]. We assume $I_{utc\_obj\_ref}$ to be zero and focus on I_{utc_dir} and I_{utc_dif}, in alignment with these previous studies. However, it is important to note that the value of $I_{utc\_obj\_ref}$ should be considered in specific situations, such as locations surrounded by buildings with white exterior walls or glass curtain walls, which can exhibit significant reflectance.

4. Experiment

Implementing the method, we collected panoramic imagery and solar irradiance data in a study area. Through this experiment, we aimed to validate the accuracy of our TCM using the dataset obtained. The following subsections provide detailed descriptions of each part of the experiment.

4.1. Study area

The experiment was conducted on the campus of National University of Singapore, which is surrounded by a residential area and situated approximately 8 kilometers from downtown Singapore (Fig. 8). Singapore's proximity to the equator results in constant and intense solar radiation exposure throughout the year. 24% of the study area, the campus, is covered by buildings, while 53% is covered by vegetation [136]. A large portion of the vegetated area is covered by tree canopies, some of which reach heights of over 20 meters. The main tree species in the area include Syzygium myrtifolium, Samanea saman, Peltophorum pterocarpum, Fagraea fragrans, and Planchonella obovata. Most of these species are evergreen, have broadleaf features, and exhibit insignificant seasonal variations. We selected 14 measurement locations within the study area. Eight of these locations were positioned approximately 2.5 meters above the ground under tree canopies, termed Under Tree Canopy (UTC) locations, while the remaining six were situated on building rooftops without any surrounding shading objects, termed Rooftop (RT) locations.

4.2. Data collection and preprocessing

4.2.1. Solar irradiance

We collected solar irradiance data through field measurements using pyranometers at UTC and RT locations during a two-month period: from March 1, 2024, to April 30, 2024. We measured global horizontal irradiance under tree crown (GHI_{utc}) at UTC locations and global horizontal irradiance on rooftops (GHI_{rt}) at RT locations. Table 1 provides details on the pyranometers used. We measured GHI_{utc} and GHI_{rt} at 1 minute intervals.

We calculated I_{dir} and I_{dif} from GHI_{rt} employing the Erbs-Driesse model [137,138], which estimates the diffuse fraction from GHI based on an empirical relationship between the diffuse fraction and GHI. We used the collected GHI_{utc} as the measured data and the calculated I_{dir} and I_{dif} as input data for our TCM in the validation process. More specifically, when estimating GHI_{utc} for a UTC location, we used I_{dir} and I_{dif} from the nearest RT location.

Fig. 9 illustrates examples of collected solar irradiance data on March 13, 2024. The values for GHI_{rt} indicate periods with significant and insignificant fluctuation. The significant fluctuations were caused by movements of local cloud covers. During periods of significant fluctuation, there could be substantial differences in cloud cover conditions even between a UTC location and the nearest RT location, potentially causing significant errors in estimations. Therefore, we excluded periods with fluctuating conditions and included only those with stable cloud conditions, using a criterion: the maximum difference in GHI_{rt} among all RT locations must be less than 100 Wm^{-2} for the preceding 30 minutes. Additionally, we excluded periods with the minimum GHI_{rt} among all RT locations below 300 Wm^{-2} to focus on sunny conditions. We calculated a 30 minutes moving average for GHI_{utc}, I_{dir}, and I_{dif} to minimize the influences of short term fluctuation of solar irradiance. As a result of this data preprocessing, the total number of data points extracted was 1058.

4.2.2. Panoramic imagery

We employed the Insta360 X3 camera to capture street-level panoramic imagery, processing these images with equirectangular projection using the Insta360 Studio software (version 5.1.0). For each UTC location in the study area, we captured a single panorama at the same height and position as the pyranometer, ensuring the center of the panorama faced north. To accurately identify the north direction, we used a compass and map during the capture process, and additionally adjusted the images post-capture using reference photos that had captured the sun at a specific time. Fig. 10 displays examples of the captured panoramic imagery.

4.3. Experiment setup for validation

To validate the performance of our TCM, we compared the accuracy of our TCM with that of the previous method, which uses only semantic segmentation and assumes the transmittance of tree canopies to be 0. Hereafter, this previous method is referred to as the "Solid Canopy Method (SCM)". We employed MAE (Mean Absolute Error), RMSE (Root Mean Square Error), and R^2 (coefficient of determination) as the indicators of performance. These were calculated using Eqs. (6), (7), and (8), respectively.

$$\mathrm{MAE}(y,\hat{y}) = \frac{1}{n}\sum_{i=1}^{n}|y_i - \hat{y}_i| \tag{6}$$

$$\mathrm{RMSE}(y,\hat{y}) = \sqrt{\frac{1}{n}\sum_{i=1}^{n}(y_i - \hat{y}_i)^2} \tag{7}$$

$$\mathrm{R}^2(y,\hat{y}) = 1 - \frac{\sum_{i=1}^{n}(y_i - \hat{y}_i)^2}{\sum_{i=1}^{n}(y_i - \bar{y})^2} \tag{8}$$

where $\hat{y}_i$ is the predicted value of the ith sample and y_i is the corresponding true value for total n samples, and $\bar{y} = \frac{1}{n}\sum_{i=1}^{n} y_i$.

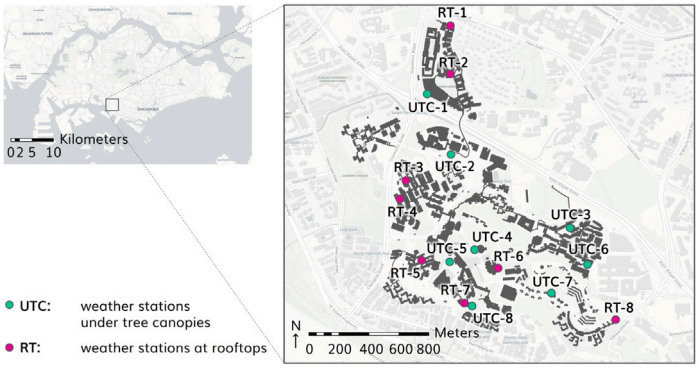

Fig. 8. Study area and measurement locations. Basemap: © OpenStreetMap contributors, © CARTO.

Table 1
Measured parameter, equipment, interval, and range.

Parameter	Equipment	Interval	Range
Global solar irradiance under tree canopy (GHI_{utc}) Wm^{-2}, Global solar irradiance on rooftops (GHI_{rt}) Wm^{-2}	Thermopile Pyranometer (LSI LASTEM, DPA863)	1 min	0 to 1500 Wm^{-2}

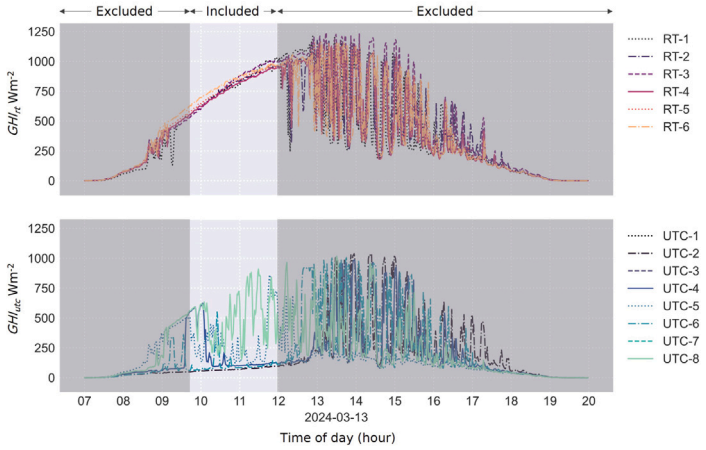

Fig. 9. Example results of solar irradiance measurements on March 13, 2024.

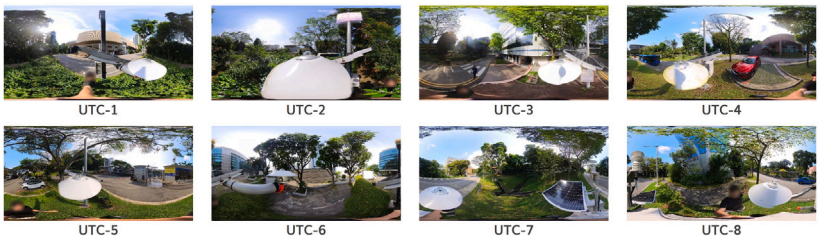

Fig. 10. Panoramic imagery of UTC locations. The center of each panorama is aligned with the north direction.

5. Results and analysis

We validated our TCM using measured solar irradiance data and captured panoramic imagery during the experiment. The following subsections detail the results of binarization, transmittance, and SVF, as well as the method's performance in estimating solar irradiance.

5.1. Binarization, transmittance and sky view factor

Fig. 11 illustrates example results of binarization. The Binarized panoramas indicate that areas segmented as 'vegetation' include a substantial proportion of white (sky) pixels, resulting in a significant difference in transmittance and SVF between our TCM and the SCM.

Fig. 12 displays example results for calculated transmittance and SVF by our TCM and the SCM. The difference in transmittance and SVF between the two methods reaches 0.8 and 0.2, respectively, at some locations. This suggests that the SCM's reliance solely on segmentation results could significantly underestimate solar irradiance, whereas our TCM could improve the performance by considering the transmittance.

Meanwhile, in one instance at UTC-8, a processing error occurred in the binarization of our TCM, where pixels representing a building behind a tree canopy were mistakenly binarized as the sky. We attribute

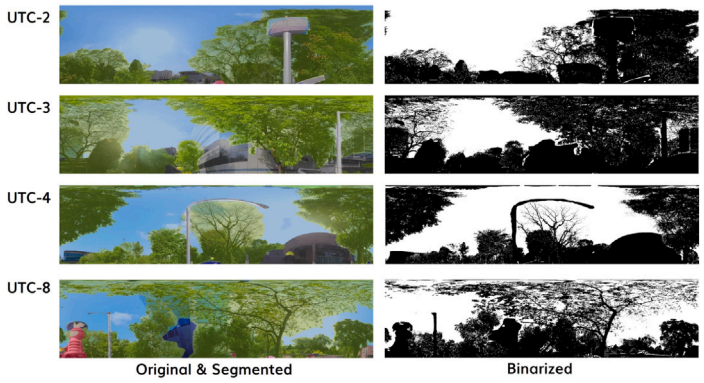

Fig. 11. Example results of binarization. Only the upper half of each result is displayed, as it impacts the calculation of the sky view factor and solar irradiance.

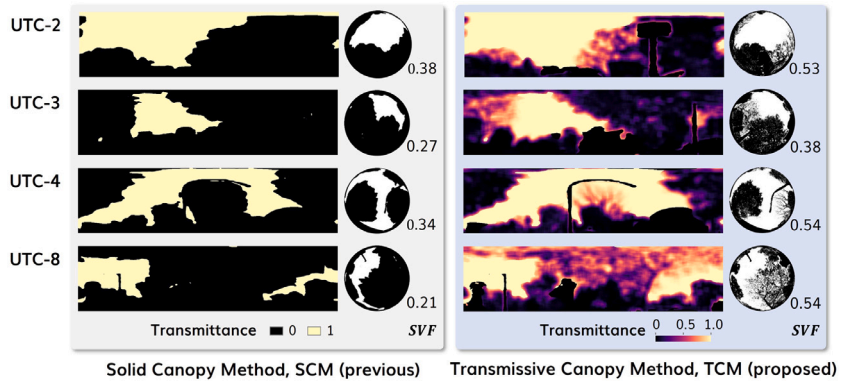

Fig. 12. Example results of sky view factor and transmittance, comparing our TCM with the SCM. Only the upper half of each result is displayed, as it impacts the calculation of the sky view factor and solar irradiance.

this processing error to the glass surface of the building, which reflects the sky and causes its pixels to have similar RGB values to those of the sky. This issue tends to arise in limited situations where buildings are obscured by trees, because our TCM can recognize buildings with glass surfaces via semantic segmentation when they are not obstructed. However, this error could still potentially lead to an overestimation in the calculation of the SVF and solar irradiance. We address this issue further in Sections 5.2 and 7.1.

Additionally, we captured supplementary panoramic imagery and calculated the SVF using both the SCM and TCM to understand the characteristics of the discrepancy between these two methods. We collected a total of 1546 supplementary panoramas in the study area. Fig. 13 illustrates a scatter plot comparing the SVF calculated by the two methods. The maximum error was 0.65, with the SCM yielding 0 and our TCM yielding 0.65. The upper fisheye photo of this case shows that the location is fully covered by tree canopies with significantly sparse leaves. This indicates that the SCM can cause a significant underestimation of the SVF in such environments, suggesting that our TCM contributes to addressing this critical gap. Meanwhile, cases with smaller errors show fewer tree canopies or tree canopies with denser leaves in their photos, indicating that the SCM can avoid significant underestimation in such situations.

In our environment, equipped with an NVIDIA GeForce RTX 4090 Ti GPU and a 12th Generation Intel® Core™ i7-1265U, the processing time of the TCM to calculate the transmittance and SVF of a single panoramic image was 0.45 seconds.

5.2. Performance of solar irradiance estimation

We calculated GHI_{utc} for each UTC location using sun position, I_{dir}, and I_{dif} from the nearest RT location. Table 2 displays the performance

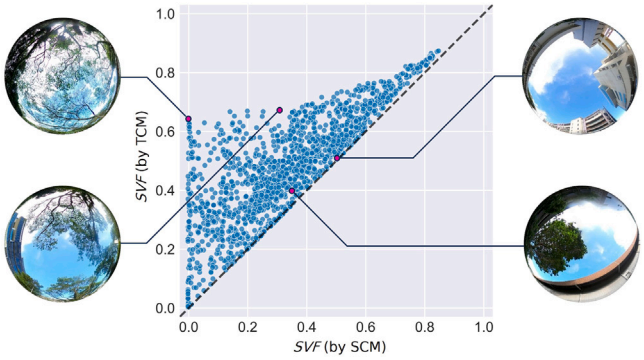

Fig. 13. Scatter plot to compare sky view factor calculated by the SCM and our TCM. Circle images are orthographic fisheye photos in an upward direction for selected plots.

metrics – MAE, RMSE, and R^2 – for all data points (overall) and for each 100 Wm^{-2} interval. For overall data points, our TCM demonstrated significant improvements over the SCM, achieving MAE of 77.8 Wm^{-2}, RMSE of 105.0 Wm^{-2}, and R^2 of 0.90, respectively. In contrast, the SCM recorded an MAE of 209 Wm^{-2}, an RMSE of 285 Wm^{-2}, and an R^2 of 0.26. The error of 77.8 Wm^{-2}, is approximately 10% of GHI in an environment without any shading objects at around noon on a sunny day in regions with tropical to temperate climates that may experience serious urban heat [139,140]. This indicates that our model achieves sufficient performance for practical applications. However, results of each data range show that the SCM performs better in the lower data range from 0 to 200 Wm^{-2}, likely due to limited underestimation because of inherently lower values. Conversely, our TCM significantly outperforms the SCM in the data range from 200 to 900 Wm^{-2}, where

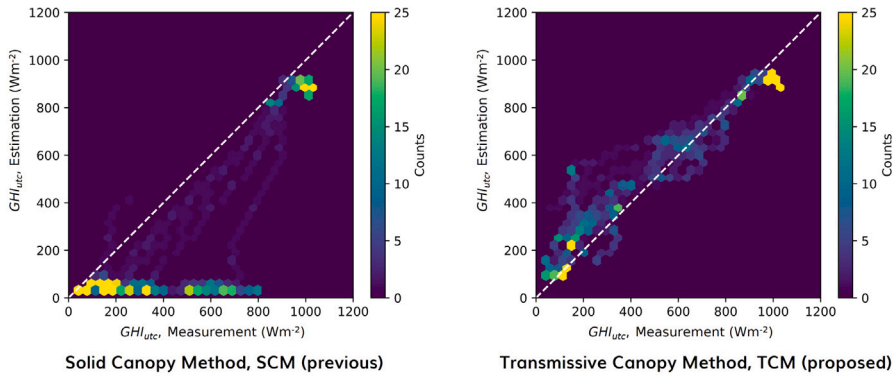

Fig. 14. Hexbin plots comparing estimated values with measured values. The left plot shows results from the SCM, while the right depicts those from our TCM.

Table 2
Comparison of performances by the SCM and our TCM.

Range	Sample size	SCM (previous)			TCM (proposed)		
(Wm^{-2})		MAE	RMSE	R^2	MAE	RMSE	R^2
Overall	1058	197.4	274.3	0.32	77.8	105	0.90
0–100	99	28.6	30.3	–	74.3	96.2	–
100–200	306	80.0	86.0	–	89.2	134.0	–
200–300	94	187.9	192.3	–	110.4	131.5	–
300–400	97	277.7	285	–	78.5	95.6	–
400–500	29	290.9	324.4	–	87.8	104.0	–
500–600	79	444.9	465.5	–	74.2	85.4	–
600–700	74	520.9	548.6	–	48.0	63.2	–
700–800	52	536.5	586.6	–	58.0	73.1	–
800–900	62	157.9	241.1	–	28.6	35.3	–
900–1000	93	80.6	85.0	–	53.3	57.0	–
1000–1100	73	131.6	132.6	–	108.5	110.1	–

the shading effect of tree canopies substantially impacted the solar irradiance under trees.

Fig. 14 illustrates the hexbin density plots of the measured data and the estimation, comparing our TCM with the SCM. The estimations by our TCM align better with the measured data than those by the SCM. This corresponds to the improvement in performance shown in Table 2. The plot for the SCM indicates significant underestimation, especially in the range from 200 to 800 Wm^{-2}. We attribute this underestimation to the underestimation of transmittance by the SCM mentioned in Section 5.1. The plot for our TCM shows a trend of overestimation particularly for GHI_{utc} values lower than 600 Wm^{-2}, which could be explained by the overestimation of transmittance due to processing errors in binarization mentioned in Section 5.1.

Based on the results above, we concluded that our TCM improves the accuracy of estimating solar irradiance under tree canopies and achieves sufficient accuracy for practical applications. However, it is important to note that the method still has room for improvement, such as correcting overestimation caused by the misrecognition of buildings behind tree canopies as the sky. Additionally, in our environment described in Section 5.1, the processing time of the TCM to calculate solar irradiance at a single timestamp from one panoramic image – excluding calculation of the transmittance and SVF – was 0.01 ms. This indicates that our TCM can be applied to real-time evaluations for broad areas if the transmittance and SVF are precomputed.

6. Use cases

We demonstrate practical applications of our TCM through two use cases: (1) High-resolution mapping of SVF and solar irradiance and (2) Walking route optimization considering sunlight exposure. The details of these use cases are provided in the following subsections.

6.1. High-resolution mapping

Taking a target field in the study area, we created maps for SVF and solar irradiance using our TCM. We used January 1, 2024, as the target date. We collected dense geo-tagged panoramic imagery in the field using a GoPro Max camera equipped with an internal GPS for geo-tagging, resulting in a total of 5731 images. Fig. 15 illustrates the locations of collected geo-tagged panoramic imagery and provides examples of the upper hemispheric fisheye images created from this panoramic imagery. The field had a building with four stories on the east side and several high trees over 10 meters tall with relatively sparse leaves, allowing some amount of solar radiation to transmit.

We created the input sun positions, I_{dir} and I_{dif} of the entire daytime, from 08:00 to 19:00 with a 5 minute interval, using the Python module 'pvlib'. Virtual clear sky conditions were assumed to calculate I_{dir} and I_{dif}, focusing on scenarios with intense solar exposure. The pvlib can simulate clear sky conditions, accounting for regional variations in atmospheric transmission of solar radiation through an airmass model and a database of regional and monthly climatological turbidity [141]. We calculated the SVF and GHI_{utc} at each location using both the SCM and ours, incorporating the collected images, input sun positions, and solar irradiance data (I_{dir} and I_{dif}). We then created maps by setting hexagonal meshes with approximately 1.0-meter width, averaging the values of locations with geo-tagged panoramas included in each mesh as its representative value.

Fig. 16 illustrates maps for SVF and accumulated GHI_{utc}, (GHI_{utc_acc}, MJm^{-2}), from 08:00 to 19:00 on the target day, comparing the SCM with ours. For the SVF, values derived from our TCM generally range from 0.4 to 0.6, whereas those from the SCM are consistently lower, mostly ranging from 0 to 0.4. Notably, areas under tree canopies exhibit significantly lower values using the SCM. We attribute this difference to our TCM's ability to accurately account for the transmittance through sparse tree canopies.

For accumulated GHI_{utc}, the map by our TCM shows higher values, around 25 MJm^{-2}, in areas without tree canopy coverage, and lower values, from 5 to 15 MJm^{-2}, in areas under tree canopies. In contrast, the map by the SCM shows much lower values compared to that of our TCM, primarily ranging from 0 to 5 MJm^{-2} in areas with tree coverage.

Fig. 17 describes high-resolution maps calculated by our TCM, which depict time-series data from 08:00 to 19:00 at one-hour intervals on the target date. These maps illustrate the diurnal changes in the distribution of solar irradiance and the movement of shaded areas caused by tree canopies and other objects such as buildings. For instance, the eastern part of the field is shaded by buildings on the east side from 10:00 to 12:00, when the azimuth angle of solar radiation is towards the east. The GHI_{utc} values in the areas shaded by buildings are significantly low, ranging from 0 to 300 Wm^{-2}, because the transmittance of buildings is essentially zero. Meanwhile, shaded areas created by tree canopies can be seen in the western part from

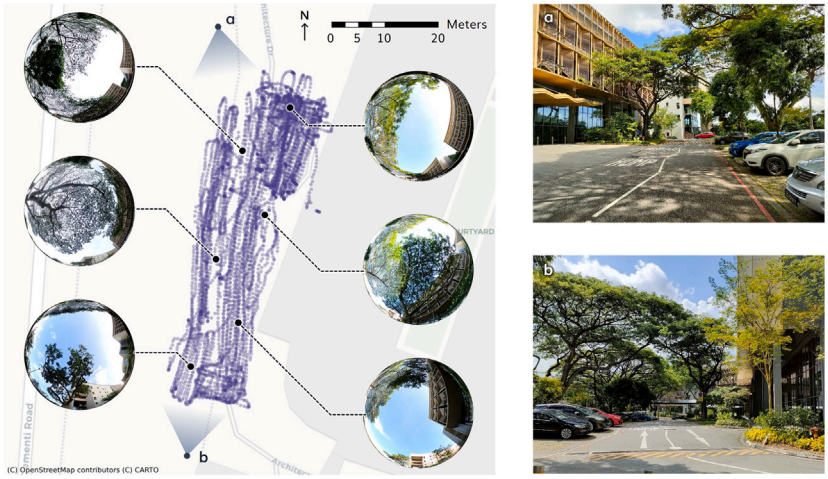

Fig. 15. Locations of geo-tagged images for high-resolution mapping, along with upper-hemispherical fisheye photos at six selected locations, and perspective photos from two viewpoints (a and b). A total of 5731 locations are depicted. Basemap: © OpenStreetMap contributors, © CARTO.

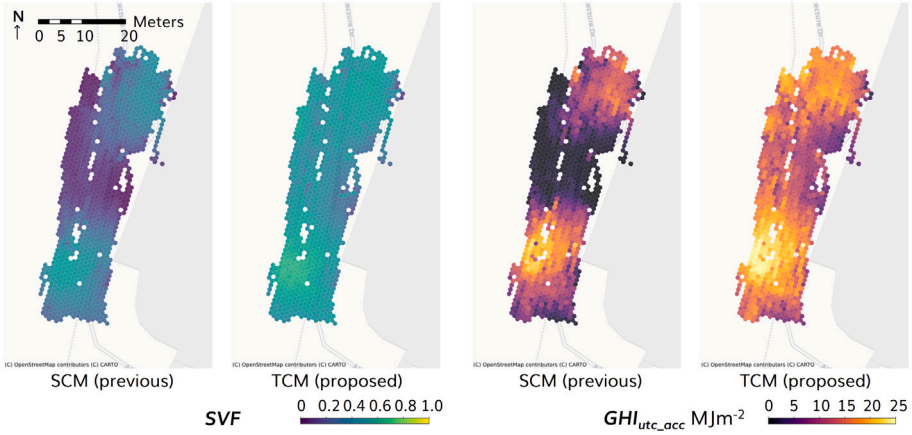

Fig. 16. High-resolution maps comparing the distribution of sky view factor and GHI_{utc_acc} using our TCM versus the SCM. Basemap: © OpenStreetMap contributors, © CARTO.

11:00 to 12:00, and in the central part from 13:00 to 16:00. The GHI_{utc} in areas shaded by tree canopies shows values ranging from 300 to 600 Wm^{-2}, which are higher compared to the values in areas shaded by buildings. This suggests that our TCM can accurately account for the differences in transmittance between tree canopies and buildings.

These maps can be used to design and locate spaces that require environments with reduced solar radiation exposure, such as terraces for cafés, rest areas in public open spaces such as parks [142–144,74], and sidewalks [145–147], and in urban agriculture and horticulture (to cultivate plants that are sensitive to direct sunlight) [148–150] — such use cases will benefit from our TCM increasingly as we face climate change-driven urban heat [151,152]. Conversely, these maps can also be utilized to design spaces that need to maximize the amount of sunlight, such as micro-scale facilities for solar power plants [153,154]. Our TCM can be applied to evaluate absorbed solar irradiance on building envelopes by using an unmanned aerial vehicle (UAV) to capture panoramic imagery aligning with vertical walls. This enables us to calculate the impact of tree shading on surface heat gain and the resulting energy consumption [155,156]. Additionally, the concept of urban digital twin – a digital representation that mirrors a real urban environment – has gained increasing attention as an efficient method for managing and planning cities among urban planners and policymakers [157–160]. Given the short processing time, the TCM can be utilized for real-time solar irradiance mapping within urban digital twins.

6.2. Walking route optimization

Different walking routes in the same area are characterized by significantly different levels of comfort, which is largely driven by solar radiation [161–163]. Our work can help in optimizing walking routes by taking into account irradiance. To demonstrate walking route optimization, we set three routes – Route-A, Route-B and, Route-C – with distances of 864, 626, and 802 meters, respectively, in the study area between a bus stop as the starting point and a library as the destination. We collected geo-tagged panoramic imagery using a GoPro Max camera along each route at two-meter intervals, resulting in a total of 1149 panoramas. We calculated GHI_{utc_acc} from 08:00 to 19:00 on a target date, January 1, 2024, along each route, using the same method as described in Section 6.1. The results are illustrated in Fig. 18. Our novel method advances the assessment of sunlight exposure along walking routes by considering transmittance through street tree canopies. From Fig. 18, we can identify spots with intense solar radiation exposure throughout the day that pose heat risks, as well as spots with less exposure. Route-A features spots with significant openness and resulting intense solar radiation exposure at the beginning; however, the route is mostly shaded by trees or buildings thereafter. Most parts of Route-B are shaded by trees and buildings; therefore, it does not have hot spots with significant solar exposure overall. For Route-C, its initial straight section is mostly covered by tree canopies and does not have significant hot spots. However, there are several spots with significant openness and sunlight exposure from

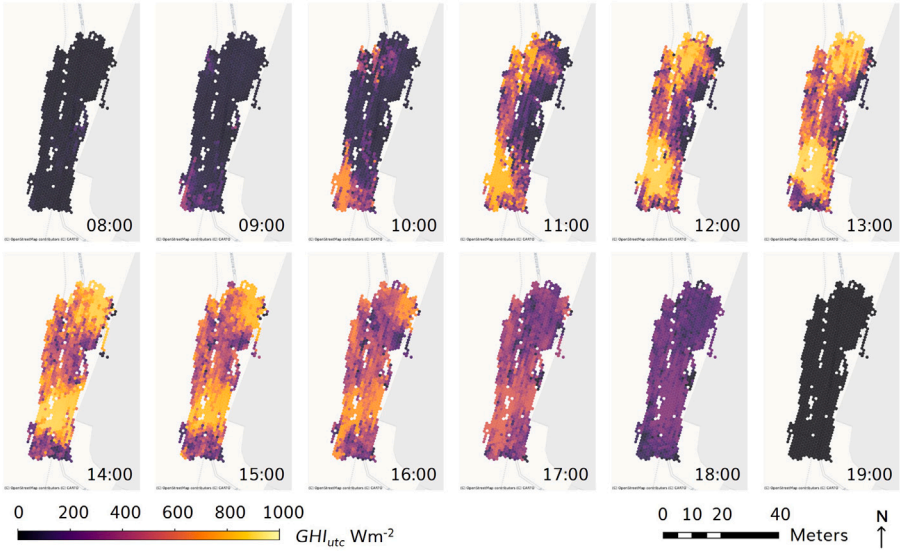

Fig. 17. Time-series high-resolution maps of GHI_{utc} from 08:00 to 19:00 on January 1, 2024 at one-hour intervals. Basemap: © OpenStreetMap contributors, © CARTO.

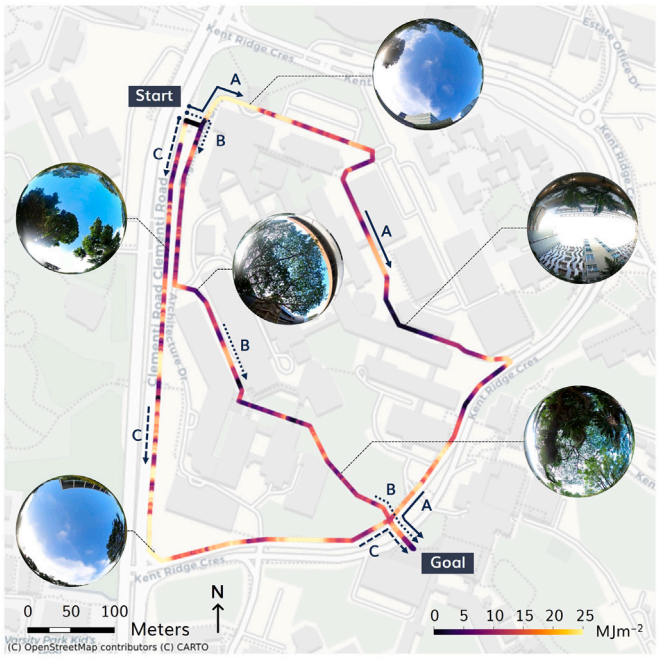

Fig. 18. Three walking routes between the starting and destination points, illustrating GHI_{utc_acc} values along each route, accompanied by upper hemispherical fisheye photos of selected locations. Basemap: © OpenStreetMap contributors, © CARTO.

the first corner until the destination. This map could be utilized for informed planning for street tree planting. Specifically, urban planners could prioritize hot spots on this map as the targets for future plantings. They could select appropriate tree species by referring to the varying shading effects offered by different species.

Additionally, we calculated accumulated GHI_{utc} during a walk along each route (GHI_{utc_walk}), setting specific departure times of 09:00, 12:00, and 15:00, and adopting a walking speed of 1.43 m/s as per a previous study [164]. For this calculation, we determined the sun position for each location using a specific timestamp, as well as the latitude and longitude of the location, which were then used as the input data for the TCM.

Fig. 19 illustrates the GHI_{utc} and GHI_{utc_walk} along each route at each departure time. It highlights the varying distributions of GHI_{utc} and the different accumulation processes of GHI_{utc_walk} during the walk depending on route and time. The GHI_{utc} and GHI_{utc_walk} at 12:00 and 15:00 are significantly higher than those at 9:00. This is due to the difference of sun position. The solar elevation at 9:00 is substantially lower than those at 12:00 and 15:00, which contribute to lower solar irradiance at 9:00. GHI_{utc_walk} of Route-A and Route-C are higher than that of Route-B across all departure times. GHI_{utc_walk} of Route-B are less than half of those of Route-A and Route-C at 9:00 and 12:00, while GHI_{utc_walk} at 15:00 indicates smaller gaps among routes. Additionally, GHI_{utc_walk} of Route-A is higher than that of Route-C at 9:00 and 15:00, while it is lower than that of Route-C at 12:00. These differences are attributed to the varying locations of shaded areas, which change with the sun position throughout the day.

These maps could be utilized to select optimal routes with lower solar radiation exposure and heat risks and to optimize the route between specific departing points and destinations, considering the spatio-temporal heterogeneity of solar irradiance. This approach could enhance the convenience and heat health safety of active mobility modes, such as walking, jogging, and biking, whether for commuting or exercise [165–168]. Such practices could result in a reduction in carbon and pollutant emissions from transportation [169,170], and improve the well-being of urban dwellers [171–173].

7. Discussion

7.1. Impact of buildings behind tree canopies

As we elaborated in Sections 5.1 and 5.2, our TCM encountered issues in the binarization process for some of the panoramas, particularly those depicting buildings obscured by tree canopies with sparse leaves. The primary issue was that the pixels representing buildings were erroneously binarized as ‘sky’, potentially leading to an overestimation of transmittance and the resulting SVF and solar irradiance. To further investigate this issue, we applied our binarization method to panoramas featuring similar conditions. Fig. 20 illustrates the binarization results for four cases: Case-1, Case-2, Case-3, and Case-4. In Case-1, which corresponds to UTC-8 in the experiment, glass and metallic surfaces reflecting the sky were binarized as ‘sky’. In Case-2, white building surfaces reflecting direct sunlight were binarized as ‘sky’. However, in Case-3 and Case-4, pixels representing building surfaces behind trees were predominantly recognized as ‘object’. This discrepancy is

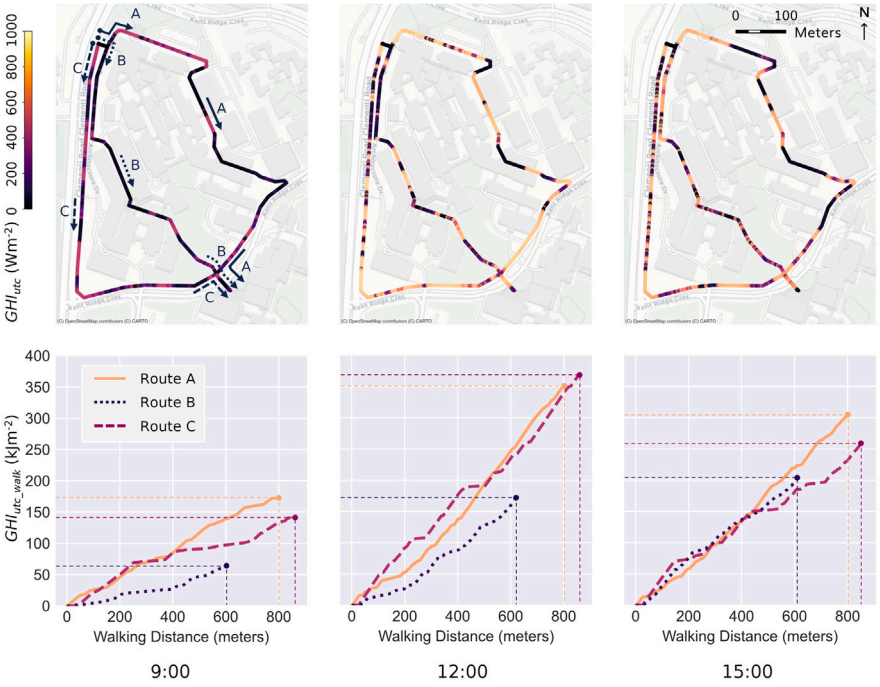

Fig. 19. Maps displaying GHI_{utc} values for each route and line charts illustrating the changes in GHI_{utc_walk} during a walk along each route, comparing results at 9:00, 12:00, 15:00 on January 1, 2024. Basemap: © OpenStreetMap contributors, © CARTO.

Fig. 20. Example results of binarization applied to panoramic imagery featuring buildings obscured by tree canopies. Pink dashed lines indicates manually drawn edges between the buildings and background.

attributed to differences in surface materials and lighting conditions. The building surfaces in Case-3, being of a brown color and not reflecting direct sunlight, were not as bright as those in Case-2. Similarly, the building surfaces in Case-4, although nearly white, did not reflect direct sunlight. It is also noteworthy that surfaces not obscured by trees in Case-2 were correctly binarized as 'object' by semantic segmentation, despite some being as bright as those misclassified as 'sky'. This suggests that the combined use of semantic segmentation and binarization contributes to improved accuracy.

These findings indicate that our TCM may exhibit reduced accuracy when analyzing panoramas depicting buildings that brightly reflect sunlight behind trees, as well as those featuring glass and metallic materials behind trees. Moreover, they suggest that avoiding conditions with strong direct sunlight when capturing panoramic imagery can enhance the accuracy of the TCM.

7.2. Impact of light conditions during panorama capturing

As discussed in Section 7.1, weather conditions and the resulting light environment can influence accuracy, and thus are important factors for our TCM. Therefore, we compared the results of binarization using panoramas captured at the same location but under different lighting conditions: (1) sunny and (2) cloudy. Fig. 21 illustrates the results of binarization along with histograms for the brightness (*pbr*) values of sky and vegetation pixels, and the ratios of object pixels in the binarized panoramas. The binarized panoramas and values of object pixel ratios show negligible differences by lighting environment, while the histograms reveal significant differences in the distribution of brightness values. This suggests that the TCM, which adjusts the brightness threshold for binarization based on the distribution features of brightness in each image, contributes to achieving a robust evaluation of transmittance and reduces the impact of lighting variations on the results.

7.3. Limitation and direction for future work

We confirmed that our TCM achieves acceptable accuracy in estimating solar irradiance under tree canopies for some practical applications. However, there are still important factors that we have not

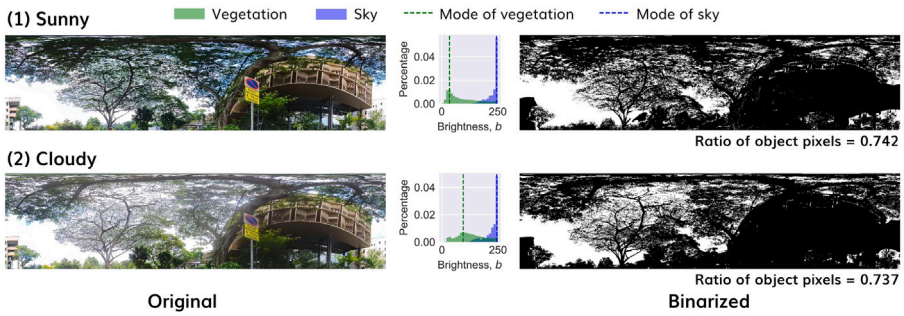

Fig. 21. Example results of binarization, including histograms of brightness values for sky and vegetation pixels, and ratios of object pixels in binarized images under (1) sunny and (2) cloudy conditions.

addressed in this study, indicating potential areas for future improvement.

For example, the TCM does not account for the solar irradiance reflected from surrounding objects such as buildings and vegetation. To assess the influence of reflected solar irradiance, it would be effective to detect the view factor and direction of such objects and determine the normal vector of each surface using depth estimation. Additionally, we have not considered the ISO sensitivity and white balance of our camera with respect to brightness. Thus, adjusting the ISO sensitivity and white balance of cameras to match the light environment during panorama capture could contribute to improving accuracy. We also have not investigated the impact of the resolution of panoramic imagery on accuracy. It is important to validate whether high-resolution improves higher accuracy, and conversely, whether low-resolution diminishes accuracy. Furthermore, the TCM does not address shading objects with transmissive properties, such as pergolas and louvers. Our approach could be extended to assess the SVF and solar irradiance beneath these structures; therefore, future studies should validate the accuracy of the TCM for these types of shading objects and apply it to more comprehensive analyses assessing the effects of diverse shading objects in urban environments.

Moreover, the TCM has only been validated on a dataset collected in our study area within a tropical climate zone. Therefore, the method might yield different accuracy for datasets that include tree canopies with significantly different morphological features from those in our dataset, such as coniferous trees. To confirm the generalization performance under diverse conditions, it is important to validate the TCM using broader datasets that include a variety of tree species.

Concerning the issue of buildings obscured by trees, future studies should develop a more accurate and detailed semantic segmentation model that can identify buildings visible between leaves as 'building'. Additionally, while we validated the TCM using measured solar irradiance, we did not validate the calculated values of transmittance and SVF themselves. Using LiDAR to measure these factors directly and validating the TCM's results with this data could enhance our understanding of its performance.

Additionally, it is important to consider transmittance when assessing the green view index [174–176]. The leaf density, or transmittance, of vegetation should substantially impact people's perception of greenery. However, previous methods that rely solely on semantic segmentation assume vegetation's transmittance is zero [177–179]. Incorporating transmittance by applying our TCM could potentially contribute to improving the accuracy of panorama-based methods to assess the green view index.

8. Conclusions

To address growing concerns regarding urban heat risks and the interest in nature-based solutions for mitigating these issues, we developed a new method, termed TCM, to evaluate SVF and solar irradiance using panoramic imagery, while considering the transmittance of tree canopies, which has not been sufficiently investigated in segmentation-based methods. Our approach advances the state of the art by enabling scalability and improving accuracy. Employing a study area situated on a university campus in Singapore, we collected data on solar irradiance and panoramic imagery, and then validated our TCM using the collected data. Additionally, we demonstrated the practical application of the TCM through two use cases: (1) two-dimensional mapping of SVF and solar irradiance in a field with tree canopies and (2) walking route optimization considering solar radiation exposure. This research resulted in the following key contributions and findings.

1. We proposed a novel method, TCM, combining techniques for semantic segmentation and binarization that can differentiate between sky and object pixels within tree canopies. This method achieves robust evaluation of transmittance without being acutely influenced by the lighting environment during panorama capturing.
2. The TCM achieved accuracy with MAE, RMSE, and R^2 values of 77.8 Wm^{-2}, 105.0 Wm^{-2} and 0.90, respectively, indicating a significant improvement compared to the previous method that did not consider the transmittance of tree canopies. This means that our TCM can more accurately evaluate the shading effect of trees, or in other words, the value of trees as a nature-based solution to urban heat.
3. The use case for two-dimensional mapping suggested potential applications for the informed design of sunlight-sensitive places such as rest areas and urban farming sites. Another use case for walking route optimization showed practical applications for finding an optimal route to avoid solar radiation exposure, considering the spatio-temporal heterogeneity of solar irradiance along each route.

CRediT authorship contribution statement

Kunihiko Fujiwara: Writing – review & editing, Writing – original draft, Visualization, Validation, Software, Methodology, Investigation, Formal analysis, Data curation, Conceptualization. **Koichi Ito:** Writing – review & editing, Software, Methodology. **Marcel Ignatius:** Writing – review & editing, Methodology, Investigation, Data curation. **Filip Biljecki:** Writing – review & editing, Supervision, Project administration, Methodology, Funding acquisition, Conceptualization.

Declaration of competing interest

The authors declare that they have no known competing financial interests or personal relationships that could have appeared to influence the work reported in this paper.

Data availability

The scripts developed for our method are openly available at a GitHub repository (https://github.com/kunifujiwara/TreeShadeMapper). The python package "tree-shade-mapper", based on the proposed method, is also openly available on PyPI (https://pypi.org/project/tree-shade-mapper/).

Declaration of Generative AI and AI-assisted technologies in the writing process

During the preparation of this work the authors used ChatGPT in order to proofread the text. After using this tool, the authors reviewed and edited the content as needed and take full responsibility for the content of the publication.

Acknowledgments

We express our gratitude to the members of the NUS Urban Analytics Lab for the valuable discussions. This research has been supported by Takenaka Corporation, Singapore, and is part of the projects (i) Large-scale 3D Geospatial Data for Urban Analytics, which is supported by the National University of Singapore under the Start Up Grant; (ii) Multi-scale Digital Twins for the Urban Environment: From Heartbeats to Cities, which is supported by the Singapore Ministry of Education Academic Research Fund Tier 1; (iii) NUS Resilience and Growth Postdoctoral Fellowship – Smart Cities and Urban Analytics, which is funded by the National Research Foundation (NRF), Singapore; (iv) Development of a Multiscale Urban Microclimate Model for NUS Campus Thermal Environment (funded by NUS); (v) Supporting Cooling NUS with BEAM initiative project (funded by the National University of Singapore and supported by the University Campus Infrastructure (UCI) and Office of the Deputy President - Research & Technology). We would like to thank the Singapore International Graduate Award (SINGA) scholarship provided by the Agency for Science, Technology, and Research (A*STAR) and the NUS.

References

[1] Y. Li, W. Ouyang, S. Yin, Z. Tan, C. Ren, Microclimate and its influencing factors in residential public spaces during heat waves: An empirical study in Hong Kong, Build. Environ. 236 (2023) 110225.
[2] M. Taleghani, A. Marshall, R. Fitton, W. Swan, Renaturing a microclimate: The impact of greening a neighbourhood on indoor thermal comfort during a heatwave in Manchester, UK, Sol. Energy 182 (2019) 245–255.
[3] R. Kotharkar, A. Ghosh, Progress in extreme heat management and warning systems: A systematic review of heat-health action plans (1995–2020), Sustainable Cities Soc. 76 (2022) 103487.
[4] H. Lee, H. Mayer, Solar elevation impact on the heat stress mitigation of pedestrians on tree-lined sidewalks of E–W street canyons — analysis under central european heat wave conditions, Urban For. Urban Green. 58 (2021) 126905.
[5] J. Xiao, T. Yuizono, Climate-adaptive landscape design: Microclimate and thermal comfort regulation of station square in the Hokuriku region, Japan, Build. Environ. 212 (2022) 108813.
[6] K. Lanza, B. Stone, Climate adaptation in cities: What trees are suitable for urban heat management? Landsc. Urban Plan. 153 (2016) 74–82.
[7] S. Eugenio Pappalardo, C. Zanetti, V. Todeschi, Mapping urban heat islands and heat-related risk during heat waves from a climate justice perspective: A case study in the municipality of Padua (Italy) for inclusive adaptation policies, Landsc. Urban Plan. 238 (2023) 104831.
[8] I. Kousis, M. Manni, A.L. Pisello, Environmental mobile monitoring of urban microclimates: A review, Renew. Sustain. Energy Rev. 169 (2022) 112847.
[9] C. Bartesaghi-Koc, P. Osmond, A. Peters, Quantifying the seasonal cooling capacity of 'green infrastructure types' (GITs): An approach to assess and mitigate surface urban heat island in Sydney, Australia, Landsc. Urban Plan. 203 (2020) 103893.
[10] O. Ananyeva, R. Emmanuel, Street trees and urban heat island in Glasgow: Mitigation through the 'avenues programme', Urban For. Urban Green. 86 (2023) 128041.
[11] A. Rafiee, E. Dias, E. Koomen, Local impact of tree volume on nocturnal urban heat island: A case study in Amsterdam, Urban For. Urban Green. 16 (2016) 50–61.
[12] S. Lee, R.J. Lee, S. Scherr, How tree canopy cover can reduce urban suicide attempts: A geospatial analysis of the moderating role of area deprivation, Landsc. Urban Plan. 230 (2023) 104606.
[13] R.M. Collins, D. Smith, B.O. Ogutu, K.A. Brown, F. Eigenbrod, R. Spake, The relative effects of access to public greenspace and private gardens on mental health, Landsc. Urban Plan. 240 (2023) 104902.
[14] M.J. Lundquist, M.R. Weisend, H.H. Kenmore, Insect biodiversity in urban tree pit habitats, Urban For. Urban Green. 78 (2022) 127788.
[15] H.M. Prather, S.M. Eppley, T.N. Rosenstiel, Urban forested parks and tall tree canopies contribute to macrolichen epiphyte biodiversity in urban landscapes, Urban For. Urban Green. 32 (2018) 133–142.
[16] M.A. Schlaepfer, B.P. Guinaudeau, P. Martin, N. Wyler, Quantifying the contributions of native and non-native trees to a city's biodiversity and ecosystem services, Urban For. Urban Green. 56 (2020) 126861.
[17] A. Fröhlich, M. Ciach, Dead tree branches in urban forests and private gardens are key habitat components for woodpeckers in a city matrix, Landsc. Urban Plan. 202 (2020) 103869.
[18] N. Khan, M.K. Jhariya, A. Raj, Urban greening toward sustainable development and sustainability, in: M. Öztürk, S.M. Khan, V. Altay, R. Efe, D. Egamberdieva, F.O. Khassanov (Eds.), Biodiversity, Conservation and Sustainability in Asia, in: Prospects and Challenges in South and Middle Asia, vol. 2, Springer International Publishing, Cham, 2022, pp. 345–373.
[19] J.B. Turner-Skoff, N. Cavender, The benefits of trees for livable and sustainable communities, Plants People Planet 1 (2019) 323–335.
[20] I. Azcarate, J.Á. Acero, L. Garmendia, E. Rojí, Tree layout methodology for shading pedestrian zones: Thermal comfort study in Bilbao (northern Iberian Peninsula), Sustainable Cities Soc. 72 (2021) 102996.
[21] J.R. Simpson, Improved estimates of tree-shade effects on residential energy use, Energy Build. 34 (2002) 1067–1076.
[22] A.A. Balogun, T.E. Morakinyo, O.B. Adegun, Effect of tree-shading on energy demand of two similar buildings, Energy Build. 81 (2014) 305–315.
[23] T. Asawa, K. Fujiwara, Estimation of sensible and latent heat fluxes of an isolated tree in Japanese summer, Bound.-Layer Meteorol. 175 (2020) 417–440.
[24] P.Y. Tan, N.H. Wong, C.L. Tan, S.K. Jusuf, K. Schmiele, Z.Q. Chiam, Transpiration and cooling potential of tropical urban trees from different native habitats, Sci. Total Environ. 705 (2020) 135764.
[25] J. Huang, F. Kong, H. Yin, A. Middel, H. Liu, X. Zheng, Z. Wen, D. Wang, Transpirational cooling and physiological responses of trees to heat, Agricult. Forest Meterol. 320 (2022) 108940.
[26] S.G. Hodder, K. Parsons, The effects of solar radiation on thermal comfort, Int. J. Biometeorol. 51 (2007) 233–250.
[27] E. Erell, D. Pearlmutter, D. Boneh, P.B. Kutiel, Effect of high-albedo materials on pedestrian heat stress in urban street canyons, Urban Clim. 10 (2014) 367–386.
[28] A. Hagishima, T. Katayama, T. Hayashi, J. Tanimoto, Numerical analysis on cooling effect of a row of trees in an urban canyon, J. Archit. Plan. 64 (1999) 83–90.
[29] Y. Ji, J. Song, P. Shen, A review of studies and modelling of solar radiation on human thermal comfort in outdoor environment, Build. Environ. 214 (2022) 108891.
[30] O. Aleksandrowicz, S. Zur, Y. Lebendiger, Y. Lerman, Shade maps for prioritizing municipal microclimatic action in hot climates: Learning from tel Aviv-Yafo, Sustainable Cities Soc. 53 (2020) 101931.
[31] O. Aleksandrowicz, Chapter 1 - mapping and management of urban shade assets: A novel approach for promoting climatic urban action, in: A. Khan, H. Akbari, F. Fiorito, S. Mithun, D. Niyogi (Eds.), Global Urban Heat Island Mitigation, Elsevier, 2022, pp. 1–27.
[32] A. Speak, L. Montagnani, C. Wellstein, S. Zerbe, The influence of tree traits on urban ground surface shade cooling, Landsc. Urban Plan. 197 (2020) 103748.
[33] M. Mõttus, M. Sulev, M. Lang, Estimation of crown volume for a geometric radiation model from detailed measurements of tree structure, Ecol. Model. 198 (2006) 506–514.
[34] W. Li, X. Mu, Using fractal dimension to correct clumping effect in leaf area index measurement by digital cover photography, Agricult. Forest Meterol. 311 (2021) 108695.
[35] R. Youngberg, Shading effects of deciduous trees, Arboric. Urban For. 9 (1983) 295–297.
[36] G. Papadakis, P. Tsamis, S. Kyritsis, An experimental investigation of the effect of shading with plants for solar control of buildings, Energy Build. 33 (2001) 831–836.
[37] K.N. Musselman, S.A. Margulis, N.P. Molotch, Estimation of solar direct beam transmittance of conifer canopies from airborne LiDAR, Remote Sens. Environ. 136 (2013) 402–415.
[38] R. Upreti, Z.-H. Wang, J. Yang, Radiative shading effect of urban trees on cooling the regional built environment, Urban For. Urban Green. 26 (2017) 18–24.
[39] W. Li, Q. Guo, S. Tao, Y. Su, VBRT: A novel voxel-based radiative transfer model for heterogeneous three-dimensional forest scenes, Remote Sens. Environ. 206 (2018) 318–335.
[40] J.P. Gastellu-Etchegorry, V. Demarez, V. Pinel, F. Zagolski, Modeling radiative transfer in heterogeneous 3-D vegetation canopies, Remote Sens. Environ. 58 (1996) 131–156.

[41] J.-F. Côté, J.-L. Widlowski, R.A. Fournier, M.M. Verstraete, The structural and radiative consistency of three-dimensional tree reconstructions from terrestrial LiDAR, Remote Sens. Environ. 113 (2009) 1067–1081.
[42] X. Zhao, J. Qi, Z. Yu, L. Yuan, H. Huang, Fine-scale quantification of absorbed photosynthetically active radiation (APAR) in plantation forests with 3D radiative transfer modeling and LiDAR data, Plant Phenomics 6 (2024) 0166.
[43] C. Miao, S. Yu, Y. Hu, H. Zhang, X. He, W. Chen, Review of methods used to estimate the sky view factor in urban street canyons, Build. Environ. 168 (2020) 106497.
[44] R. Carrasco-Hernandez, A.R.D. Smedley, A.R. Webb, Using urban canyon geometries obtained from google street view for atmospheric studies: Potential applications in the calculation of street level total shortwave irradiances, Energy Build. 86 (2015) 340–348.
[45] S.M. Ivanova, C.A. Gueymard, Simulation and applications of cumulative anisotropic sky radiance patterns, Sol. Energy 178 (2019) 278–294.
[46] S. Blankenstein, W. Kuttler, Impact of street geometry on downward longwave radiation and air temperature in an urban environment, Meteorol. Z. 13 (2004) 373–379.
[47] X. He, S. Miao, S. Shen, J. Li, B. Zhang, Z. Zhang, X. Chen, Influence of sky view factor on outdoor thermal environment and physiological equivalent temperature, Int. J. Biometeorol. 59 (2015) 285–297.
[48] M. Asgarzadeh, A. Lusk, T. Koga, K. Hirate, Measuring oppressiveness of streetscapes, Landsc. Urban Plan. 107 (2012) 1–11.
[49] M. Asgarzadeh, T. Koga, K. Hirate, M. Farvid, A. Lusk, Investigating oppressiveness and spaciousness in relation to building, trees, sky and ground surface: A study in tokyo, Landsc. Urban Plan. 131 (2014) 36–41.
[50] Y. Zhang, S. Li, R. Dong, H. Deng, X. Fu, C. Wang, T. Yu, T. Jia, J. Zhao, Quantifying physical and psychological perceptions of urban scenes using deep learning, Land Use Policy 111 (2021) 105762.
[51] X. Zhao, Y. Lu, G. Lin, An integrated deep learning approach for assessing the visual qualities of built environments utilizing street view images, Eng. Appl. Artif. Intell. 130 (2024) 107805.
[52] W. Qiu, Z. Zhang, X. Liu, W. Li, X. Li, X. Xu, X. Huang, Subjective or objective measures of street environment, which are more effective in explaining housing prices? Landsc. Urban Plan. 221 (2022) 104358.
[53] Y. Ogawa, T. Oki, C. Zhao, Y. Sekimoto, C. Shimizu, Evaluating the subjective perceptions of streetscapes using street-view images, Landsc. Urban Plan. 247 (2024) 105073.
[54] K. Nakagawa, Estimation of the sky view-factor from a fish-eye lens image, considering the anisotropy of the downward longwave radiation, J. Meteorol. Soc. Jpn. 66 (1988) 903–912.
[55] K. Blennow, Sky view factors from high-resolution scanned fish-eye lens photographic negatives, J. Atmos. Ocean. Technol. 12 (1995) 1357–1362.
[56] D.G. Steyn, The calculation of view factors from fisheye-lens photographs: Research note, Atmos.-Ocean 18 (1980) 254–258.
[57] Z.-H. Jiao, H. Ren, X. Mu, J. Zhao, T. Wang, J. Dong, Evaluation of four sky view factor algorithms using digital surface and elevation model data, Earth Space Sci. 6 (2019) 222–237.
[58] F.F. Sönmez, H. Ziar, O. Isabella, M. Zeman, Fast and accurate ray-casting-based view factor estimation method for complex geometries, Sol. Energy Mater. Sol. Cells 200 (2019) 109934.
[59] C. Chatzipoulka, R. Compagnon, J. Kaempf, M. Nikolopoulou, Sky view factor as predictor of solar availability on building façades, Sol. Energy 170 (2018) 1026–1038.
[60] T. Honjo, T.-P. Lin, Y. Seo, Sky view factor measurement by using a spherical camera, J. Agric. Meteorol. 75 (2019) 59–66.
[61] W. Hong, K. Choi, E. Lee, S. Im, M. Heo, Analysis of GNSS performance index using feature points of sky-view image, IEEE Trans. Intell. Transp. Syst. 15 (2014) 889–895.
[62] K. Du, J. Ning, L. Yan, How long is the sun duration in a street canyon? — — analysis of the view factors of street canyons, Build. Environ. 172 (2020) 106680.
[63] M. Deng, W. Yang, C. Chen, Z. Wu, Y. Liu, C. Xiang, Street-level solar radiation mapping and patterns profiling using baidu street view images, Sustainable Cities Soc. 75 (2021) 103289.
[64] F.-Y. Gong, Z.-C. Zeng, E. Ng, L.K. Norford, Spatiotemporal patterns of street-level solar radiation estimated using google street view in a high-density urban environment, Build. Environ. 148 (2019) 547–566.
[65] F.-Y. Gong, Z.-C. Zeng, F. Zhang, X. Li, E. Ng, L.K. Norford, Mapping sky, tree, and building view factors of street canyons in a high-density urban environment, Build. Environ. 134 (2018) 155–167.
[66] F. Biljecki, T. Zhao, X. Liang, Y. Hou, Sensitivity of measuring the urban form and greenery using street-level imagery: A comparative study of approaches and visual perspectives, Int. J. Appl. Earth Obs. Geoinf. 122 (2023) 103385.
[67] K.-T. Huang, S.-R. Yang, A. Matzarakis, T.-P. Lin, Identifying outdoor thermal risk areas and evaluation of future thermal comfort concerning shading orientation in a traditional settlement, Sci. Total Environ. 626 (2018) 567–580.
[68] S. Coccolo, J. Kämpf, J.-L. Scartezzini, D. Pearlmutter, Outdoor human comfort and thermal stress: A comprehensive review on models and standards, Urban Clim. 18 (2016) 33–57.
[69] S. Rowlinson, A. Yunyanjia, B. Li, C. Chuanjingju, Management of climatic heat stress risk in construction: A review of practices, methodologies, and future research, Accid. Anal. Prev. 66 (2014) 187–198.
[70] L.S.H. Lee, P.K. Cheung, C.K.W. Fung, C.Y. Jim, Improving street walkability: Biometeorological assessment of artificial-partial shade structures in summer sunny conditions, Int. J. Biometeorol. 64 (2020) 547–560.
[71] M. Tomasi, M. Nikolopoulou, R. Giridharan, M. Löve, C. Ratti, Definition of a maximum threshold of direct solar radiation exposure for pedestrians of diverse walking abilities, Int. J. Biometeorol. 68 (2024) 17–31.
[72] D. Lai, Z. Lian, W. Liu, C. Guo, W. Liu, K. Liu, Q. Chen, A comprehensive review of thermal comfort studies in urban open spaces, Sci. Total Environ. 742 (2020) 140092.
[73] V. Cheng, E. Ng, Thermal comfort in urban open spaces for hong kong, Archit. Sci. Rev. 49 (2006) 236–242.
[74] B.J. Walkosz, M.D. Scott, D.B. Buller, P.A. Andersen, L. Beck, G.R. Cutter, Prevalence of sun protection at outdoor recreation and leisure venues at resorts in North America, Am. J. Health Educ. 48 (2017) 90–99.
[75] J. Hofierka, J. Kaňuk, Assessment of photovoltaic potential in urban areas using open-source solar radiation tools, Renew. Energy 34 (2009) 2206–2214.
[76] J.D. Mondol, Y.G. Yohanis, B. Norton, Solar radiation modelling for the simulation of photovoltaic systems, Renew. Energy 33 (2008) 1109–1120.
[77] G.M. Heisler, Measurements of solar radiation on vertical surfaces in the shade of individual trees, in: B.A. Hutchison, B.B. Hicks (Eds.), The Forest-Atmosphere Interaction: Proceedings of the Forest Environmental Measurements Conference Held At Oak Ridge, Tennessee, October 23–28, 1983, Springer Netherlands, Dordrecht, 1985, pp. 319–335.
[78] J.P. Hardy, R. Melloh, G. Koenig, D. Marks, A. Winstral, J.W. Pomeroy, T. Link, Solar radiation transmission through conifer canopies, Agricult. Forest Meterol. 126 (2004) 257–270.
[79] W. Ni, X. Li, C.E. Woodcock, J.L. Roujean, et al., Transmission of solar radiation in boreal conifer forests: Measurements and models, J. Geophys. Res. (1997).
[80] J. Konarska, F. Lindberg, A. Larsson, S. Thorsson, B. Holmer, Transmissivity of solar radiation through crowns of single urban trees—application for outdoor thermal comfort modelling, Theor. Appl. Climatol. 117 (2014) 363–376.
[81] Á. Takács, M. Kiss, Á. Gulyás, E. Tanács, N. Kántor, Solar permeability of different tree species in Szeged, Hungary, Geogr. Pannonica 20 (2016) 32–41.
[82] S. Yoshida, A. Nakai, R. Ooka, Effects of growth and types of trees on leaf area density and optical depth on tree canopy : Study on method to evaluate the shading effect of street tree on solar radiation based on field observation, J. Environ. Eng. Trans. AIJ 71 (2006) 103–110.
[83] R. Nishikawa, M. Shukuya, Development of a method for estimating the shading effect of the crown of a single tree, J. Archit. Plan. Trans. AIJ 65 (2000) 29–35.
[84] I. Kousis, I. Pigliautile, A.L. Pisello, Intra-urban microclimate investigation in urban heat island through a novel mobile monitoring system, Sci. Rep. 11 (2021) 9732.
[85] G. Sonohat, P. Balandier, F. Ruchaud, Predicting solar radiation transmittance in the understory of even-aged coniferous stands in temperate forests, Ann. For. Sci. 61 (2004) 629–641.
[86] T. Perot, A. Mårell, N. Korboulewsky, V. Seigner, P. Balandier, Modeling and predicting solar radiation transmittance in mixed forests at a within-stand scale from tree species basal area, Forest Ecol. Manag. 390 (2017) 127–136.
[87] T.E. Morakinyo, L. Kong, K.K.-L. Lau, C. Yuan, E. Ng, A study on the impact of shadow-cast and tree species on in-canyon and neighborhood's thermal comfort, Build. Environ. 115 (2017) 1–17.
[88] E. Kumakura, K. Nakaohkubo, A. Hoyano, Numerical analysis of solar transmittance of a deciduous tree crown, J. Jpn. Inst. Landsc. Archit. 73 (2010) 573–576.
[89] H. Kobayashi, D.D. Baldocchi, Y. Ryu, Q. Chen, S. Ma, J.L. Osuna, S.L. Ustin, Modeling energy and carbon fluxes in a heterogeneous oak woodland: A three-dimensional approach, Agricult. Forest Meterol. 152 (2012) 83–100.
[90] H. Kobayashi, Y. Ryu, D.D. Baldocchi, J.M. Welles, J.M. Norman, On the correct estimation of gap fraction: How to remove scattered radiation in gap fraction measurements? Agricult. Forest Meterol. 174-175 (2013) 170–183.
[91] T. Asawa, A. Hoyano, K. Nakaohkubo, Thermal design tool for outdoor spaces based on heat balance simulation using a 3D-CAD system, Build. Environ. 43 (2008) 2112–2123.
[92] D. Sun, Visual quality evaluation of urban landscape based on computer vision technology, in: W. Gao (Ed.), Digital Analysis of Urban Structure and Its Environment Implication, Springer Nature Singapore, Singapore, 2023, pp. 139–169.
[93] R.J. Cureau, I. Pigliautile, A.L. Pisello, Seasonal and diurnal variability of a water body's effects on the urban microclimate in a coastal city in Italy, Urban Clim. 49 (2023) 101437.
[94] L. Zeng, J. Lu, W. Li, Y. Li, A fast approach for large-scale sky view factor estimation using street view images, Build. Environ. 135 (2018) 74–84.
[95] D. Muñoz, B. Beckers, G. Besuievsky, G. Patow, A technique for massive sky view factor calculations in large cities, Int. J. Remote Sens. 39 (2018) 4040–4058.
[96] A. Matzarakis, M. Gangwisch, D. Fröhlich, RayMan and SkyHelios model, in: M. Palme, A. Salvati (Eds.), Urban Microclimate Modelling for Comfort and Energy Studies, Springer International Publishing, Cham, 2021, pp. 339–361.

[97] M. Béland, J.-L. Widlowski, R.A. Fournier, A model for deriving voxel-level tree leaf area density estimates from ground-based LiDAR, Environ. Model. Softw. 51 (2014) 184–189.
[98] M. Detto, G.P. Asner, H.C. Muller-Landau, O. Sonnentag, Spatial variability in tropical forest leaf area density from multireturn LiDAR and modeling, J. Geophys. Res. Biogeosci. 120 (2015) 294–309.
[99] M. Alonzo, B. Bookhagen, J.P. McFadden, A. Sun, D.A. Roberts, Mapping urban forest leaf area index with airborne LiDAR using penetration metrics and allometry, Remote Sens. Environ. 162 (2015) 141–153.
[100] H. Oshio, T. Asawa, A. Hoyano, S. Miyasaka, Estimation of the leaf area density distribution of individual trees using high-resolution and multi-return airborne LiDAR data, Remote Sens. Environ. 166 (2015) 116–125.
[101] Y. Lin, G. West, Retrieval of effective leaf area index (LAIe) and leaf area density (LAD) profile at individual tree level using high density multi-return airborne LiDAR, Int. J. Appl. Earth Obs. Geoinformation 50 (2016) 150–158.
[102] F. Hosoi, K. Omasa, Factors contributing to accuracy in the estimation of the woody canopy leaf area density profile using 3D portable LiDAR imaging, J. Exp. Bot. 58 (2007) 3463–3473.
[103] J.J. Richardson, L.M. Moskal, S.-H. Kim, Modeling approaches to estimate effective leaf area index from aerial discrete-return LIDAR, Agricult. Forest Meterol. 149 (2009) 1152–1160.
[104] I. Moorthy, J.R. Miller, B. Hu, J. Chen, Q. Li, Retrieving crown leaf area index from an individual tree using ground-based LiDAR data, Can. J. Remote Sens. 34 (2008) 320–332.
[105] J. Arnó, A. Escolà, J.M. Vallès, J. Llorens, R. Sanz, J. Masip, J. Palacín, J.R. Rosell-Polo, Leaf area index estimation in vineyards using a ground-based LiDAR scanner, Precis. Agric. 14 (2013) 290–306.
[106] B.N. Bailey, W.F. Mahaffee, Rapid measurement of the three-dimensional distribution of leaf orientation and the leaf angle probability density function using terrestrial LiDAR scanning, Remote Sens. Environ. 194 (2017) 63–76.
[107] G. Zheng, L. Monika Moskal, Leaf orientation retrieval from terrestrial laser scanning (TLS) data, IEEE Trans. Geosci. Remote Sens. 50 (2012) 3970–3979.
[108] Z. Zhang, X. Ma, H. Guan, K. Zhu, J. Feng, S. Yu, A method for calculating the leaf inclination of soybean canopy based on 3D point clouds, Int. J. Remote Sens. 42 (2021) 5719–5740.
[109] Z. Li, X. Feng, J. Sun, C. Li, W. Yu, Z. Fang, STMRT: A simple tree canopy radiative transfer model for outdoor mean radiant temperature, Build. Environ. 228 (2023) 109846.
[110] I. Jonckheere, S. Fleck, K. Nackaerts, B. Muys, P. Coppin, M. Weiss, F. Baret, Review of methods for in situ leaf area index determination: Part I. Theories, sensors and hemispherical photography, Agricult. Forest Meterol. 121 (2004) 19–35.
[111] S. Garrigues, N.V. Shabanov, K. Swanson, J.T. Morisette, F. Baret, R.B. Myneni, Intercomparison and sensitivity analysis of leaf area index retrievals from LAI-2000, AccuPAR, and digital hemispherical photography over croplands, Agricult. Forest Meterol. 148 (2008) 1193–1209.
[112] G.W. Frazer, C.D. Canham, K.P. Lertzman, Imaging software to extract canopy structure and gap light transmission indices from true-colour fisheye photographs, users manual and program ..., 1999, Gap Light Analyzer (GLA). Version.
[113] S. Watanabe, K. Nagano, J. Ishii, T. Horikoshi, Evaluation of outdoor thermal comfort in sunlight, building shade, and pergola shade during summer in a humid subtropical region, Build. Environ. 82 (2014) 556–565.
[114] A. Peeters, L. Shashua-Bar, S. Meir, R.R. Shmulevich, Y. Caspi, M. Weyl, W. Motzafi-Haller, N. Angel, A decision support tool for calculating effective shading in urban streets, Urban Clim. 34 (2020) 100672.
[115] A.I. Palmero-Marrero, A.C. Oliveira, Effect of louver shading devices on building energy requirements, Appl. Energy 87 (2010) 2040–2049.
[116] G. Datta, Effect of fixed horizontal louver shading devices on thermal perfomance of building by TRNSYS simulation, Renew. Energy 23 (2001) 497–507.
[117] X. Li, C. Ratti, Mapping the spatio-temporal distribution of solar radiation within street canyons of boston using google street view panoramas and building height model, Landsc. Urban Plan. 191 (2019) 103387.
[118] M. Wang, J. Haworth, H. Chen, Y. Liu, Z. Shi, Investigating the potential of crowdsourced street-level imagery in understanding the spatiotemporal dynamics of cities: A case study of walkability in inner London, Cities 153 (2024) 105243.
[119] C. Wang, S.E. Antos, L.M. Triveno, Automatic detection of unreinforced masonry buildings from street view images using deep learning-based image segmentation, Autom. Constr. 132 (2021) 103968.
[120] H. He, X. Lin, Y. Yang, Y. Lu, Association of street greenery and physical activity in older adults: A novel study using pedestrian-centered photographs, Urban For. Urban Green. 55 (2020) 126789.
[121] S.-N. Kim, H. Lee, Capturing reality: Validation of omnidirectional video-based immersive virtual reality as a streetscape quality auditing method, Landsc. Urban Plan. 218 (2022) 104290.
[122] Y. Ao, J. Wang, M. Zhou, R.C. Lindenbergh, M.Y. Yang, Fully convolutional networks for street furniture identification in panorama images, in: ISPRS Geospatial Week 2019 (Volume XLII-2/W13) - 10–14 2019, Enschede, the Netherlands, vol. XLII-2-W13, Copernicus GmbH, 2019, pp. 13–20.
[123] Z. Liu, A. Yang, M. Gao, H. Jiang, Y. Kang, F. Zhang, T. Fei, Towards feasibility of photovoltaic road for urban traffic-solar energy estimation using street view image, J. Clean. Prod. 228 (2019) 303–318.
[124] A. Middel, J. Lukasczyk, R. Maciejewski, M. Demuzere, M. Roth, Sky view factor footprints for urban climate modeling, Urban Clim. 25 (2018) 120–134.
[125] R. Kou, B. Yang, Z. Dong, F. Liang, S. Yang, Mapping the spatio-temporal visibility of global navigation satellites in the urban road areas based on panoramic imagery, Int. J. Digit. Earth 14 (2021) 807–820.
[126] T. Jonas, C. Webster, G. Mazzotti, J. Malle, HPEval: A canopy shortwave radiation transmission model using high-resolution hemispherical images, Agricult. Forest Meterol. 284 (2020) 107903.
[127] N. Otsu, A threshold selection method from gray-level histograms, IEEE Trans. Syst. Man Cybern. 9 (1979) 62–66.
[128] B. Cheng, I. Misra, A.G. Schwing, A. Kirillov, R. Girdhar, Masked-attention mask transformer for universal image segmentation, 2022, arXiv:2112.01527.
[129] M. Cordts, M. Omran, S. Ramos, T. Rehfeld, M. Enzweiler, R. Benenson, U. Franke, S. Roth, B. Schiele, The cityscapes dataset for semantic urban scene understanding, in: Proc. of the IEEE Conference on Computer Vision and Pattern Recognition, CVPR, 2016.
[130] W.F. Holmgren, C.W. Hansen, M.A. Mikofski, Pvlib python: A python package for modeling solar energy systems, J. Open Source Softw. 3 (2018) 884.
[131] I. Reda, A. Andreas, Solar position algorithm for solar radiation applications, Sol. Energy 76 (2004) 577–589.
[132] D. Heim, D. Knera, A novel photometric method for the determination of reflected solar irradiance in the built environment, Renew. Sustain. Energy Rev. 137 (2021) 110451.
[133] J.A. Villena Del Carpio, D.L. Marinoski, G. Trichês, R. Lamberts, J.V.S. de Melo, Urban pavements used in brazil: Characterization of solar reflectance and temperature verification in the field, Sol. Energy 134 (2016) 72–81.
[134] D. Hu, M. Liu, Y. Di, C. Yu, Y. Wang, USRT: A solar radiative transfer model dedicated to estimating urban 3D surface reflectance, Urban Sci. 4 (2020) 66.
[135] R.H. Grant, G.M. Heisler, W. Gao, M. Jenks, Ultraviolet leaf reflectance of common urban trees and the prediction of reflectance from leaf surface characteristics, Agricult. Forest Meterol. 120 (2003) 127–139.
[136] University Campus Infrastructure, Annual Report 2020, Technical Report, National University of Singapore, 2020.
[137] D.G. Erbs, S.A. Klein, J.A. Duffie, Estimation of the diffuse radiation fraction for hourly, daily and monthly-average global radiation, Sol. Energy 28 (1982) 293–302.
[138] A. Driesse, A.R. Jensen, R. Perez, A continuous form of the perez diffuse sky model for forward and reverse transposition, Sol. Energy 267 (2024) 112093.
[139] J.L. De Souza, R.M. Nicácio, M.A.L. Moura, Global solar radiation measurements in Maceió, Brazil, Renew. Energy 30 (2005) 1203–1220.
[140] Y.A. Eltbaakh, M.H. Ruslan, M.A. Alghoul, M.Y. Othman, K. Sopian, M.I. Fadhel, Measurement of total and spectral solar irradiance: Overview of existing research, Renew. Sustain. Energy Rev. 15 (2011) 1403–1426.
[141] P. Ineichen, R. Perez, A new airmass independent formulation for the linke turbidity coefficient, Sol. Energy 73 (2002) 151–157.
[142] S. Chen, F. Biljecki, Automatic assessment of public open spaces using street view imagery, Cities 137 (2023) 104329.
[143] T.R. Palomo Amores, J. Sánchez Ramos, M. Guerrero Delgado, D. Castro Medina, A. Cerezo-Narváéz, S. Álvarez Domínguez, Effect of green infrastructures supported by adaptative solar shading systems on livability in open spaces, Urban For. Urban Green. 82 (2023) 127886.
[144] A. Middel, N. Selover, B. Hagen, N. Chhetri, Impact of shade on outdoor thermal comfort—A seasonal field study in tempe, arizona, Int. J. Biometeorol. 60 (2016) 1849–1861.
[145] N. Langenheim, M. White, N. Tapper, S.J. Livesley, D. Ramirez-Lovering, Right tree, right place, right time: A visual-functional design approach to select and place trees for optimal shade benefit to commuting pedestrians, Sustainable Cities Soc. 52 (2020) 101816.
[146] Y. Azegami, M. Imanishi, K. Fujiwara, H. Kusaka, Effects of solar radiation in the streets on pedestrian route choice in a city during the summer season, Build. Environ. 235 (2023) 110250.
[147] M. Tomasi, M. Nikolopoulou, R. Giridharan, M. Löve, A design workflow for effective solar shading of pedestrian paths, Build. Environ. 261 (2024) 111718.
[148] S. Song, J.C. Cheong, J.S.H. Lee, J.K.N. Tan, Z. Chiam, S. Arora, K.J.Q. Png, J.W.C. Seow, F.W.S. Leong, A. Palliwal, F. Biljecki, A. Tablada, H.T.W. Tan, Home gardening in singapore: A feasibility study on the utilization of the vertical space of retrofitted high-rise public housing apartment buildings to increase urban vegetable self-sufficiency, Urban For. Urban Green. 78 (2022) 127755.
[149] Y. Shao, J. Li, Z. Zhou, Z. Hu, F. Zhang, Y. Cui, H. Chen, The effects of vertical farming on indoor carbon dioxide concentration and fresh air energy consumption in office buildings, Build. Environ. 195 (2021) 107766.
[150] T. Li, Q. Yang, Advantages of diffuse light for horticultural production and perspectives for further research, Front. Plant Sci. 6 (2015) 704.
[151] C. Wang, Z. Ren, Y. Guo, P. Zhang, S. Hong, Z. Ma, W. Hong, X. Wang, Assessing urban population exposure risk to extreme heat: Patterns, trends, and implications for climate resilience in China (2000–2020), Sustainable Cities Soc. 103 (2024) 105260.

[152] H. Sun, Y. Chen, K. Li, S. Gao, Spatio–temporal assessment of heat health risk in chinese metropolitan cities based on the modified multi-indicators coupled risk framework, Sustainable Cities Soc. 108 (2024) 105451.
[153] K. Sunderland, M. Narayana, G. Putrus, M. Conlon, Levelised cost of energy analysis: A comparison of urban (micro) wind turbines and solar PV systems, in: 2016 51st International Universities Power Engineering Conference, UPEC, IEEE, 2016, pp. 1–6.
[154] J. Taminiau, J. Byrne, City-scale urban sustainability: Spatiotemporal mapping of distributed solar power for New York city, Wiley Interdiscip. Rev. Energy Environ. 9 (2020) e374.
[155] C.-M. Hsieh, J.-J. Li, L. Zhang, B. Schwegler, Effects of tree shading and transpiration on building cooling energy use, Energy Build. 159 (2018) 382–397.
[156] R. Berry, S.J. Livesley, L. Aye, Tree canopy shade impacts on solar irradiance received by building walls and their surface temperature, Build. Environ. 69 (2013) 91–100.
[157] T. Deng, K. Zhang, Z.-J. m. Shen, A systematic review of a digital twin city: A new pattern of urban governance toward smart cities, J. Manag. Sci. Eng. 6 (2021) 125–134.
[158] F. Jiang, L. Ma, T. Broyd, W. Chen, H. Luo, Digital twin enabled sustainable urban road planning, Sustainable Cities Soc. 78 (2022) 103645.
[159] B. Lei, P. Janssen, J. Stoter, F. Biljecki, Challenges of urban digital twins: A systematic review and a delphi expert survey, Autom. Constr. 147 (2023) 104716.
[160] M. Ignatius, J. Lim, B. Gottkehaskamp, K. Fujiwara, C. Miller, F. Biljecki, Digital twin and wearables unveiling pedestrian comfort dynamics and walkability in cities, in: ISPRS TC IV (WG IV/9)
19th 3D GeoInfo Conference 2024-1–3 2024, Vigo, Spain, vol. X-4-W5-2024, Copernicus GmbH, 2024, pp. 195–202.
[161] P. Liu, T. Zhao, J. Luo, B. Lei, M. Frei, C. Miller, F. Biljecki, Towards human-centric digital twins: Leveraging computer vision and graph models to predict outdoor comfort, Sustainable Cities Soc. 93 (2023) 104480.
[162] H. Zhao, S. Wang, Y. Zhang, L. Zhao, Y. Zhai, R.D. Brown, L. Jin, R. Wu, The effect of solar radiation on pedestrian thermal comfort: A climate chamber experiment, Build. Environ. 245 (2023) 110869.
[163] J. Li, J. Niu, C.M. Mak, Influences of variable thermal exposures on walking thermal comfort in hot summer - physio-psychological responses, Build. Environ. 239 (2023) 110346.
[164] R.W. Bohannon, A. Williams Andrews, Normal walking speed: A descriptive meta-analysis, Physiotherapy 97 (2011) 182–189.
[165] A. Pimpinella, A.E.C. Redondi, M. Cesana, Walk this way! an IoT-based urban routing system for smart cities, Comput. Netw. 162 (2019) 106857.
[166] Y. Huang, S. Eom, T. Suzuki, Preference-based jogging route selection in downtown Tokyo, Cities Health 1–15.
[167] S. Guhathakurta, G. Zhang, M.K. Panguluru, R. Sivakumar, Walk route: A new methodology to find the optimal walking route in the city of atlanta, in: S. Geertman, F. Toppen, J. Stillwell (Eds.), Planning Support Systems for Sustainable Urban Development, Springer Berlin Heidelberg, Berlin, Heidelberg, 2013, pp. 309–325.
[168] K. Ito, F. Biljecki, Assessing bikeability with street view imagery and computer vision, Transp. Res. C 132 (2021) 103371.
[169] Y. Van Fan, S. Perry, J.J. Klemeš, C.T. Lee, A review on air emissions assessment: Transportation, J. Clean. Prod. 194 (2018) 673–684.
[170] F.N.D. Ribeiro, A.S. Umezaki, J.B. Chiquetto, I. Santos, P.G. Machado, R.M. Miranda, P.S. Almeida, A.F. Simões, D. Mouette, A.R. Leichsenring, H.M. Ueno, Impact of different transportation planning scenarios on air pollutants, greenhouse gases and heat emission abatement, Sci. Total Environ. 781 (2021) 146708.
[171] P. Schnohr, T.S. Kristensen, E. Prescott, H. Scharling, Stress and life dissatisfaction are inversely associated with jogging and other types of physical activity in leisure time–the copenhagen city heart study, Scand. J. Med. Sci. Sports 15 (2005) 107–112.
[172] A.C. Gatrell, Therapeutic mobilities: Walking and 'steps' to wellbeing and health, Health Place 22 (2013) 98–106.
[173] E. Pantelaki, E. Maggi, D. Crotti, Mobility impact and well-being in later life: A multidisciplinary systematic review, Res. Transp. Econ. 86 (2021) 100975.
[174] X. Li, C. Zhang, W. Li, R. Ricard, Q. Meng, W. Zhang, Assessing street-level urban greenery using google street view and a modified green view index, Urban For. Urban Green. 14 (2015) 675–685.
[175] S. Yu, B. Yu, W. Song, B. Wu, J. Zhou, Y. Huang, J. Wu, F. Zhao, W. Mao, View-based greenery: A three-dimensional assessment of city buildings' green visibility using floor green view index, Landsc. Urban Plan. 152 (2016) 13–26.
[176] J. Yang, L. Zhao, J. Mcbride, P. Gong, Can you see green? Assessing the visibility of urban forests in cities, Landsc. Urban Plan. 91 (2009) 97–104.
[177] W. Zhang, H. Zeng, Spatial differentiation characteristics and influencing factors of the green view index in urban areas based on street view images: A case study of Futian district, Shenzhen, China, Urban For. Urban Green. 93 (2024) 128219.
[178] D. Ki, S. Lee, Analyzing the effects of green view index of neighborhood streets on walking time using google street view and deep learning, Landsc. Urban Plan. 205 (2021) 103920.
[179] T. Aikoh, R. Homma, Y. Abe, Comparing conventional manual measurement of the green view index with modern automatic methods using Google street view and semantic segmentation, Urban For. Urban Green. 80 (2023) 127845.